ROBUST PROBABILISTIC QUANTUM INFORMATION PROCESSING WITH ATOMS, PHOTONS, AND ATOMIC ENSEMBLES

L.-M. DUAN and C. MONROE

FOCUS, MCTP, and Department of Physics, University of Michigan,
Ann Arbor, MI 48109-1040, USA

Abstract

In this article, we review several new approaches to scalable and robust quantum communication, state engineering, and quantum computation. We consider the use of atomic ensembles, linear optical elements, and trapped ions for this purpose, all having significant experimental simplifications compared to conventional systems. These new approaches are based on probabilistic entanglement of quantum bits, where the dominant source of error is the (typically small) probability of entanglement success per attempt. By exploiting the properties of this particular noise

419

process, we can design scalable quantum network schemes that are inherently in-
sensitive to the noise, resulting in error-correction thresholds that are much more
forgiving than any conventional threshold requirement. We review several such
types of schemes in different contexts, and show their close relations with the current
experimental implementations of scalable quantum information processing. Exper-
imental progress along these approaches will be briefly remarked, especially in a
system of trapped atomic ions.

1. Introduction

Quantum information systems hold great promise for superfast computation and
secure communication (Nielsen and Chuang, 2000). However, practical quantum
hardware can be highly susceptible to external noise and decoherence, leading
to quantum information errors. This is especially true during quantum logic op-
erations, where interactions between quantum bits must be controlled with great
precision. Quantum error correction of some form will therefore be essential for
reliable quantum information processing (Shor, 1995; Steane, 1997). The fun-
damental quantum error threshold theorem (Preskill, 1998) states that the error
per quantum operation must be less than a particular (small) threshold value for
effective error correction. However, noise levels in current experimental systems
are typically orders of magnitude larger than fault-tolerant thresholds for arbitrary
quantum errors. An alternative approach to general error correction is to exploit
the properties of the noise itself to design schemes that either automatically cor-
rect the dominant source of noise, or lead to specific types of errors that can be
more easily corrected later.

In this article, we review several schemes for reliable quantum communication,
state engineering, and quantum computation, that can tolerate very high levels
of experimental noise. The experimental systems in our consideration range from
atomic ensembles, to photonic systems (such as the spontaneous parametric down
conversion or cavity QED systems), and to individual trapped atoms or ions. The
precise physical sources of noise in these different systems can be quite different,
and there are a number of system-specific properties which are discussed. How-
ever, in spite of these differences, the dominant noise in these systems share very
similar properties. All of these schemes involve photons, and the dominant source
of noise is always some type of photon loss, related to "quantum leakage" errors,
where the state of the physical system continuously leaks outside of the logical
Hilbert space that carries the quantum information. Because of this similarity in
the noise properties, we can identify very efficient error-correction methods for

all of these systems and achieve scalability in quantum communication, state engineering, and quantum computation in the face of high noise levels.

In the next section, we review the scalable quantum communication scheme using atomic ensembles first proposed in Duan et al. (2001). This scheme implements a quantum repeater architecture (Briegel et al., 1998), although does not require the dominant noise to be below a stringent threshold value. The recent remarkable experimental progress using this approach is discussed briefly (Kuzmich et al., 2003; Van der Wal et al., 2003; Chou et al. 2004, 2005; Matsukevich and Kuzmich, 2004; Blinov et al., 2004; Balic et al., 2005; Chaneliere et al., 2005; Eisaman et al., 2005; Black et al., 2005; Manz et al., 2006; Riedmatten et al., 2006; Matsukevich et al., 2006). In Section 3, we review a recent scheme for quantum state engineering with linear optics (Bodiya and Duan, **?**), where entangled "graph states" can be created in a scalable fashion with realistic linear optical systems under current technology. Finally, in the last section, we review approaches to scalable quantum computation and networking based on probabilistic entangling gates (Duan et al., 2005; Barrett and Kok, 2005), and the implementation of these types of gates using trapped ions (Duan et al., 2006) and cavity QED systems (Duan et al., 2005). Some recent trapped ion experiments are described that represent an initial step in achieving such gate operations (Madsen et al., 2006; Maunz et al., 2006).

2. Quantum Communication with Atomic Ensembles

2.1. Quantum Repeaters for Scalable Communication

The communication of quantum information over remote distances is essential for realizing quantum networks and secretly transferring messages by means of quantum cryptography. The key resource in quantum communication is the generation of nearly perfect entangled states between distant sites. Such states can be used then to implement secure quantum cryptography (Ekert, 1991) or to transfer arbitrary quantum messages (Bennett et al., 1993). Realistic schemes for quantum communication are based on photonic channels, as photons are the only viable particles that can be transmitted with high speeds over long distances. To overcome the inevitable signal attenuation in the channel, the concept of entanglement purification was invented (Bennett et al., 1997). However, entanglement purification does not fully solve the problem for long-distance quantum communication. Due to the exponential decay of the entanglement with the channel length, one needs an exponentially large number of partially entangled states to obtain one highly entangled state, which means that for a sufficiently long distance the task becomes nearly impossible.

The idea of a quantum repeater was proposed by Briegel et al. (1998) to mitigate the exponential decay of fidelity with distance. In principle, quantum

repeaters allow the overall communication fidelity to approach unity, with the communication time growing only polynomially with the transmission distance. In analogy with fault-tolerant quantum computing (Preskill, 1998), the quantum repeater is a concatenated (nested) entanglement purification protocol for communication systems. The idea is to divide the transmission channel into many segments, with the length of each segment comparable to the channel attenuation length. Entanglement is first generated and purified for each segment, then the purified entanglement is extended to longer lengths by connecting two adjacent segments through the entanglement swapping protocol (Bennett et al., 1993). Following this, the overall entanglement decreases and must be purified again. These rounds of entanglement swapping and purification can be repeated until nearly perfect entangled states are created between two distant sites. Similar to fault tolerant quantum computation, the conventional quantum repeater protocol requires the noise per quantum operation (such as a local gate operation for the entanglement purification or a quantum transmission operation) to be below a certain threshold value. However, this threshold value is considerably less stringent than qubit error-correction thresholds for quantum computing. Error thresholds for quantum repeaters are typically estimated to be at the $\sim$1% level.

In this section, we review the implementation scheme of quantum repeaters proposed by Duan, Lukin, Cirac, and Zoller (2001) (DLCZ). This scheme has a nested architecture similar to the original quantum repeater protocol (Briegel et al., 1998), but it uses a very different noise reduction method. Instead of explicit entanglement purifications at each step, the DLCZ scheme features inherent fault tolerance. In this scheme, the dominant noise is first classified in the proposed experimental system (e.g., atomic ensembles). Based on the properties of this noise, the entanglement generation, connection (swapping), and application schemes are designed so that each step of this protocol has some function of built-in entanglement purification. Through this built-in entanglement purification, each step partially removes the noise from all of the previous steps, and as a result, the noise accumulates much more slowly. The effect of the remaining noise is removed by the last step of entanglement application, and we can then prove that one has an overall efficient scaling. Because there is no need for additional steps of explicit entanglement purification, this scheme overcomes stringent error threshold requirements, and can tolerate important experimental noise at much higher levels. For instance, with the DLCZ scheme, photon detector efficiencies can be around 50% or even lower without significantly influencing the overall scaling of the protocol. In the conventional approach (Briegel et al., 1998), even with a forgiving error-correction threshold at the percent level, photon detector efficiencies (and any other sources of photon loss) must still be larger than 99% which is still considered challenging with current technology. So, inherent fault tolerance to high levels of noise is the essential feature of this DLCZ scheme. Such a property is critical for the recent remarkable experimental progress using

this approach (Kuzmich et al., 2003; Van der Wal et al., 2003; Chou et al., 2004, 2005; Matsukevich and Kuzmich, 2004; Blinov et al., 2004; Balic et al., 2005; Chaneliere et al., 2005; Eisaman et al., 2005; Black et al., 2005; Manz et al., 2006; Riedmatten et al., 2006; Matsukevich et al., 2006).

2.2. COLLECTIVE ENHANCEMENT IN INTERACTION BETWEEN LIGHT AND ATOMIC ENSEMBLES

The DLCZ scheme proposes atomic ensembles as nodes for quantum repeaters. The atomic ensemble contains a large number of identical neutral atoms, which might consist of either laser-cooled atoms (Kuzmich et al., 2003; Chou et al., 2004; Black et al., 2005; Manz et al., 2006; Matsukevich et al., 2006), or a room-temperature vapor (Van der Wal et al., 2003; Julsgaard et al., 2001). The motivation of using atomic ensembles instead of single-particles for quantum information processing is two-fold: first, laser manipulation of atomic ensembles without separate addressing of individual atoms is simpler than the laser manipulation of single particles; and second, the use of the atomic ensembles allows for collective effects resulting from many-atom coherences to enhance the signal-to-noise ratio, which is critical for increasing efficiencies of some quantum information protocols (Fleischhauer and Lukin, 2000; Duan et al., 2000, 2001; Julsgaard et al., 2001). The collective enhancement in atomic ensembles and its applications in quantum information has been reviewed in several recent articles (Cirac et al., 2001; Lukin, 2003).

In the DLCZ scheme, a different level configuration is used, and the collective enhancement effect for this configuration becomes more subtle, as shown in detail in Duan et al. (2002). The atomic ensemble consists of a cloud of N_a identical atoms with the relevant level structure shown in Fig. 1A. A pair of stable lower states $|g\rangle$ and $|s\rangle$ can correspond, for instance, to hyperfine or Zeeman sublevels of electronic ground state of alkali atoms. The relevant coherence between the levels $|g\rangle$ and $|s\rangle$ can be maintained for a sufficiently long time, which provides the desired quantum memory. All the atoms are initially prepared in the ground state $|g\rangle$ through optical pumping.

The ensemble is then illuminated by a weak pumping laser pulse which drives the transition $|g\rangle \rightarrow |e\rangle$ with a large detuning Δ, and we look at the spontaneous emission light from the transition $|e\rangle \rightarrow |s\rangle$, whose polarization and/or frequency are assumed to be different from that of the pumping laser. The pumping laser is directed onto all the atoms in the focusing area so that each atom has nearly the same small probability to be excited into the state $|s\rangle$ through the Raman transition. (It is a simple matter to extend the analysis to inhomogeneous couplings where different atoms have different excitation probabilities by appropriately redefining the collective atomic mode.)
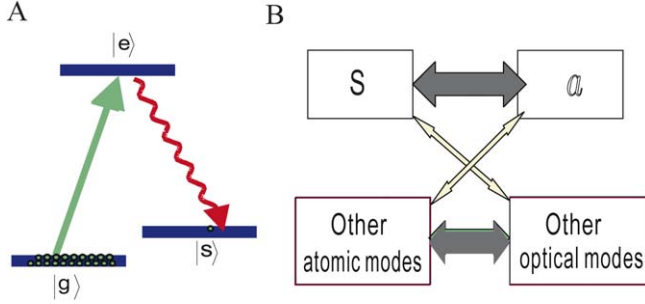
FIG. 1. (A) The relevant atomic level structure with ground and metastable states $|g\rangle$ and $|s\rangle$, and excited state $|e\rangle$. (B) Correlations between the atomic modes of an atomic ensemble (left), and the free-space optical modes (right). The symmetric atomic mode S is predominantly correlated with the forward scattered optical mode a, with only weak correlations to other optical modes that account for spontaneous emission noise. Likewise, the forward scattered mode a is only weakly correlated with other (nonsymmetric) atomic modes (see Duan et al., 2002).

With the above Raman transition, the corresponding spontaneous photon from each atom can be emitted in any direction given by the dipole emission pattern, and without any selection on the photonic or atomic state, there will be no collective enhancement effect that gives rise to directional emission. (In the weak-pumping regime considered here, we neglect effects of superradiant emission.) However, considering the atomic gas with many atoms, we can define collective atomic modes. If we look at a particular atomic mode, it gets correlated with a well-defined photon mode that is directional in space. For instance, the symmetric atomic mode S (resulting from homogeneous excitation) is defined as

$$S \equiv \left(1/\sqrt{N_a}\right) \sum_{i=1}^{N_a} |g\rangle_i \langle s|. \tag{1}$$

This atomic mode is correlated with a special optical spontaneous emission mode a (called the signal mode) which is essentially collinear with the pumping laser. The signal mode a can be written by expanding the spontaneous emission field in plane wave modes:

$$a = \int f_{\mathbf{k}}^* a_{\mathbf{k}} \, d^3 \mathbf{k}, \tag{2}$$

where $a_{\mathbf{k}}$ represents the plane wave mode with the wave vector $\mathbf{k}$. The operators $a_{\mathbf{k}}$ satisfy the standard commutation relations $[a_{\mathbf{k}}, a_{\mathbf{k}'}^\dagger] = \delta(\mathbf{k} - \mathbf{k}')$, and $f_{\mathbf{k}}^*$ is the normalized signal mode function whose explicit form depends on the pumping laser profile and the geometry of the atomic ensemble, as specified in Duan et al. (2002). The modes S and a are correlated with each other: if the atom collection is excited into the symmetric collective mode S, the accompanying spontaneous

emission photon is be emitted into the signal mode a, and vice versa. There are many other atomic modes in the ensemble and optical modes in the spontaneous emission field, and these background modes can be correlated with each other in a complicated pattern that depends on details concerning the thermal motion of the atoms. However, the correlation between the particular modes S and a is maintained even with a large degree of atomic thermal motion. In experiments with cold atomic ensembles, the correlation pattern between the atomic and the optical modes gets simplified as the atomic thermal motional effect is minimized, and correlations between other atomic and optical modes can be used, where the spontaneous emission photon is non-collinear with the pumping pulse (Balic et al., 2005). Due to density fluctuations in the atomic gas, the modes S and a can still get weakly correlated with the other atomic and optical modes, inducing so-called spontaneous emission noise. This noise vanishes as the atomic gas becomes optically thick. The explicit characterization of the noise can be found in Duan et al. (2002). The correlation picture between different atomic and optical modes is shown schematically in Fig. 1B.

The application of this system to quantum communication comes from the correlation between the modes S and a, which can both be selectively detected. The mode a is directional in space with a well-defined mode structure, so it can be coupled into a single-mode optical fiber and then detected by a single-photon detector. The excitation in the atomic mode S can be subsequently transferred into a directional optical photon with a repumping laser pulse (Fleischhauer and Lukin, 2000; Cirac et al., 2001; Liu et al., 2001; Phillips et al., 2001) and then can be similarly detected by a single-photon detector coupled through a fiber. With this detection method, we can neglect the other atomic and optical modes as they have no influence on the above measurements, and we are left with an effective two-mode problem. The pure correlation between the modes S and a can then be used to generate entanglement between two distant atomic ensembles, which eventually leads to realization of quantum repeaters as described in the next section.

2.3. Entanglement Generation, Connection, and Entanglement-Based Communication Schemes

To realize long-distance quantum communication, first we need to entangle two atomic ensembles within the channel attenuation length, and then connect different segments of entanglement to generate a long-distance entangled state. We follow the same approach as in Duan et al. (2001).

The entanglement generation scheme is based on photon interference at photodetectors, which critically uses the fault-tolerance property of photon detection. With a weak pumping laser pulse, the state of the atomic and the optical modes S and a can be written in the form (Duan et al., 2002)

$$|\phi\rangle = |0_a\rangle|0_p\rangle + \sqrt{p_c}S^\dagger a^\dagger|0_a\rangle|0_p\rangle + O(p_c), \tag{3}$$
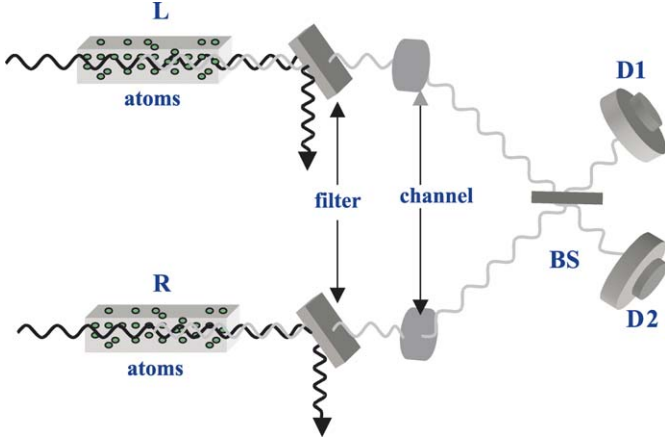
FIG. 2. Schematic setup for generating entanglement between the two atomic ensembles L and R (see Duan et al., 2001). The two ensembles are pencil shaped and illuminated by the synchronized classical laser pulses. The forward-scattered Stokes pulses are collected after the filters (polarization and frequency selective) and interfered at a 50%–50% beam splitter (*BS*) after the transmission channels, with the outputs detected respectively by two single-photon detectors D_1 and D_2. If there is a click in D_1 or D_2, the process is finished and we successfully generate entanglement between the ensembles L and R. Otherwise, we first apply a repumping pulse to drive the transition $|2\rangle \to |3\rangle$ on the ensembles L and R to reset the state of the ensembles back to the ground state $|0\rangle_a^L \otimes |0\rangle_a^R$, then the same classical laser pulses as the first round drive the transition $|1\rangle \to |3\rangle$ and we detect again the forward-scattering Stokes pulses after the beam splitter. This process is repeated until finally we have a click in the D_1 or D_2 detector.

where $p_c \ll 1$ is a small excitation probability, and $|0_a\rangle$ and $|0_p\rangle$ denote the vacuum (no excitation) state of the modes S and a_s, respectively.

Now we explain how to use this setup to generate entanglement between two distant ensembles L and R using the configuration shown in Fig. 2. Here, two laser pulses excite both ensembles simultaneously, and the whole system is described by the state $|\phi\rangle_L \otimes |\phi\rangle_R$, where $|\phi\rangle_L$ and $|\phi\rangle_R$ are given by Eq. (3) with all the operators and states distinguished by the subscript L or R. The forward scattered Stokes signal from both ensembles is combined at the beam splitter and a photodetector click in either D_1 or D_2 measures the combined radiation from two samples, $a_+^\dagger a_+$ or $a_-^\dagger a_-$ with $a_\pm = (a_L \pm e^{i\varphi} a_R)/\sqrt{2}$. Here, φ denotes an unknown difference of the phase shifts in the two-side channels. We can also assume that φ has an imaginary part to account for the possible asymmetry of the setup, which will also be corrected automatically in the scheme. But the setup asymmetry can be easily made very small, and for simplicity of expressions we assume that φ is real in the following. Conditional on the detector click, we should apply a_+ or a_- to the whole state $|\phi\rangle_L \otimes |\phi\rangle_R$, and the projected state of the ensembles L and R is nearly maximally entangled with the form (neglecting the high-order

terms of order p_c),

$$|\Psi_\varphi\rangle_{LR}^\pm = \left(S_L^\dagger \pm e^{i\varphi} S_R^\dagger\right)\big/\sqrt{2}\,|0_a\rangle_L|0_a\rangle_R. \tag{4}$$

The probability for getting a click is given by p_c for each round, so we need repeat the process about $1/p_c$ times for a successful entanglement preparation, and the average preparation time is approximately given by t_Δ/p_c, where t_Δ is the duration of each pumping cycle. The states $|\Psi_r\rangle_{LR}^+$ and $|\Psi_r\rangle_{LR}^-$ can be easily transformed to each other by a simple local phase shift. Without loss of generality, we assume in the following that the entangled state $|\Psi_r\rangle_{LR}^+$ is generated.

The presence of noise modifies the projected state of the ensemble to

$$\rho_{LR}(c_0, \varphi) = \frac{1}{c_0 + 1}\big(c_0|0_a 0_a\rangle_{LR}\langle 0_a 0_a| + |\Psi_\varphi\rangle_{LR}^+\langle\Psi_\varphi|\big), \tag{5}$$

where the "vacuum" coefficient c_0 is determined by the dark count rates of the photon detectors. It is seen below that any state in the form of Eq. (5) will be purified automatically to a maximally entangled state in the entanglement-based communication schemes. We therefore call this state an effective maximally entangled (EME) state with the vacuum coefficient c_0 determining the purification efficiency.

After successful generation of entanglement within the attenuation length, we now extend the quantum communication distance. This is done through entanglement swapping with the configuration shown in Fig. 3. Suppose that we start with two pairs of the entangled ensembles described by the state $\rho_{LI_1} \otimes \rho_{I_2 R}$, where ρ_{LI_1} and $\rho_{I_2 R}$ are given by Eq. (5). In the ideal case, the setup shown in Fig. 3 measures the quantities corresponding to operators $S_\pm^\dagger S_\pm$ with $S_\pm = (S_{I_1} \pm S_{I_2})/\sqrt{2}$. If the measurement is successful (i.e., one of the detectors registers one photon), we prepare the ensembles L and R into another EME state. The new φ-parameter is given by $\varphi_1 + \varphi_2$, where φ_1 and φ_2 denote the old φ-parameters for the two segment EME states. Even in the presence of realistic noise such as photon loss, an EME state is still created after a detector click. The noise only influences the success probability to get a click and the new vacuum coefficient in the EME state. The above method for connecting entanglement can be continued to extend the communication over an arbitrary distance.

After an EME state has been established between two distant sites, we would like to use it in the communication protocols, such as for quantum teleportation, cryptography, or Bell inequality detection. It is not obvious that the EME state [Eq. (5)], which is entangled in the Fock basis, is useful for these tasks since in the Fock basis it is experimentally hard to do certain single-bit operations. In the following we show how the EME states can indeed be used to realize all these protocols with simple experimental configurations.

Quantum cryptography and the Bell inequality detection are achieved with the setup shown by Fig. 4. The state of the two pairs of ensembles is expressed as
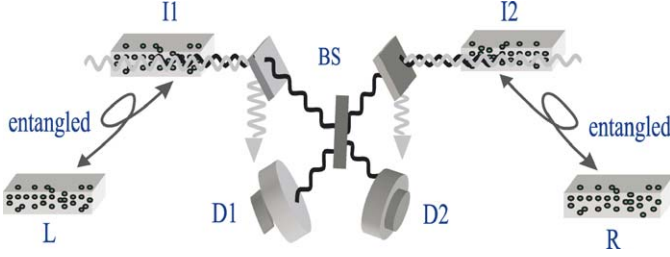
FIG. 3. Illustration for the entanglement connection (swapping) (see Duan et al., 2001). We have two pairs of ensembles L, I_1 and I_2, R distributed at three sites L, I and R. Each of the ensemble-pairs L, I_1 and I_2, R is prepared in an EME state in the form of Eq. (3). The excitations in the collective modes of the ensembles I_1 and I_2 are transferred simultaneously to the optical excitations by the repumping pulses applied to the atomic transition $|2\rangle \rightarrow |3\rangle$, and the stimulated optical excitations, after a 50%–50% beam splitter, are detected by single-photon detectors D_1 and D_2. If either D_1 or D_2 clicks, the protocol is successful and an EME state in the form of Eq. (3) is established between the ensembles L and R with a doubled communication distance. Otherwise, the process fails, and we need to repeat the previous entanglement generation and swapping until finally we have a click in D_1 or D_2, that is, until the protocol finally succeeds.

$\rho_{L_1 R_1} \otimes \rho_{L_2 R_2}$, where $\rho_{L_i R_i}$ ($i = 1, 2$) denote the same EME state with the vacuum coefficient c_n if we have carried out the entanglement connection n times. The φ-parameters in $\rho_{L_1 R_1}$ and $\rho_{L_2 R_2}$ are the same provided that the two states are established over the same stationary channels. We register only the coincidences of the two-side detectors, so the protocol is successful only if there is a click on each side. Under this condition, the vacuum components in the EME states, together with the state components $S_{L_1}^\dagger S_{L_2}^\dagger |vac\rangle$ and $S_{R_1}^\dagger S_{R_2}^\dagger |vac\rangle$, where $|vac\rangle$ denotes the ensemble state $|0_a 0_a 0_a 0_a\rangle_{L_1 R_1 L_2 R_2}$, have no contributions to the experimental results. So, for the measurement scheme shown by Fig. 4, the
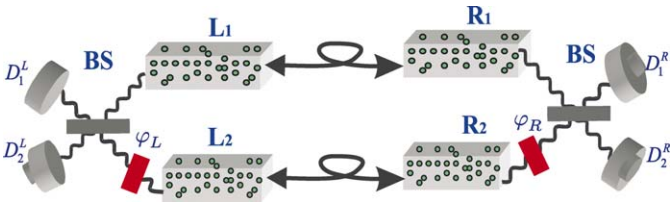
FIG. 4. Schematic setup for the realization of quantum cryptography and Bell inequality detection (see Duan et al., 2001). Two pairs of ensembles L_1, R_1 and L_2, R_2 have been prepared in the EME states. The collective atomic excitations on each side are transferred to the optical excitations, which, respectively after a relative phase shift φ_L or φ_R and a 50%–50% beam splitter, are detected by the single-photon detectors D_1^L, D_2^L and D_1^R, D_2^R. We look at the four possible coincidences of D_1^R, D_2^R with D_1^L, D_2^L, which are functions of the phase difference $\varphi_L - \varphi_R$. Depending on the choice of φ_L and φ_R, this setup can realize both the quantum cryptography and the Bell inequality detection.

ensemble state $\rho_{L_1 R_1} \otimes \rho_{L_2 R_2}$ is effectively equivalent to the following "polariza-tion" maximally entangled (PME) state (the terminology of "polarization" comes from an analogy to the optical case)

$$|\Psi\rangle_{PME} = \left(S_{L_1}^\dagger S_{R_2}^\dagger + S_{L_2}^\dagger S_{R_1}^\dagger\right)/\sqrt{2} \,|vac\rangle. \tag{6}$$

The success probability for the projection from $\rho_{L_1 R_1} \otimes \rho_{L_2 R_2}$ to $|\Psi\rangle_{PME}$ (i.e., the probability to get a click on each side) is given by $1/[2(c_n + 1)^2]$. One can also check that in Fig. 4, the phase shift φ_Λ ($\Lambda = L$ or R) together with the corresponding beam splitter operation are equivalent to a single-bit rotation in the basis $\{|0\rangle_\Lambda \equiv S_{\Lambda_1}^\dagger |0_a 0_a\rangle_{\Lambda_1 \Lambda_2}, |1\rangle_\Lambda \equiv S_{\Lambda_2}^\dagger |0_a 0_a\rangle_{\Lambda_1 \Lambda_2}\}$ with the rotation angle $\theta = \varphi_\Lambda/2$. Since we have the effective PME state and we can perform the desired single-bit rotations in the corresponding basis, it is clear how to use this facility to realize quantum cryptography, Bell inequality detection, as well as teleportation (see Duan et al., 2001 for details).

2.4. BUILT-IN ENTANGLEMENT PURIFICATION AND SCALING OF THE COMMUNICATION EFFICIENCY

It is remarkable that all the steps of entanglement generation, connection, and application schemes described above are robust to practical noise. Now we ana-lyze the built-in entanglement purification in each step, which, combined together, makes the whole scheme noise resilient.

In the entanglement generation, the dominant noise is photon loss, which in-cludes the contributions from the channel attenuation, spontaneous emission in the atomic ensembles (which results in the population of the collective atomic mode correlated with the accompanying photon going to other directions), the coupling inefficiency of the Stokes light into and out of the channel, and the inefficiency of the single-photon detectors. The loss probability is denoted by $1 - \eta_p$ with the overall efficiency $\eta_p = \eta_p' e^{-L_0/L_{att}}$, where we have separated the exponential channel attenuation factor (with channel attenuation length L_{att}) from other noise contributions η_p' that are independent of the communication dis-tance L_0. The photon loss decreases the success probability for getting a detector click from p_c to $\eta_p p_c$, but it has no influence on the resulting EME state. Due to this noise, the entanglement preparation time is now written as $T_0 \sim t_\Delta/(\eta_p p_c)$. The second source of noise comes from the dark counts of the single-photon detectors. The dark count gives a detector click, but without population of the collective atomic mode, so it contributes to the vacuum coefficient in the EME state. If the dark count comes with a probability p_{dc} over the time interval t_Δ, the vacuum coefficient is given by $c_0 = p_{dc}/(\eta_p p_c)$, which is typically much smaller than unity since the Raman transition rate is much larger than the dark count rate. The final source of noise, which influences the fidelity to get the EME state, is

caused by the event that more than one atom are excited to the collective mode S whereas there is only one click in D_1 or D_2. The conditional probability for that event is given by p_c, so we can estimate the infidelity $\bar{F}_0 \equiv 1 - F_0$ for the entanglement generation by

$$\bar{F}_0 \sim p_c. \tag{7}$$

Note that by decreasing the excitation probability p_c, the infidelity can be made closer to zero with the price of a longer entanglement preparation time T_0. This is the basic idea of the entanglement purification. So, in this scheme, the confirmation of the click from the single-photon detector generates and purifies entanglement at the same time.

In the entanglement swapping step, the dominant noise remains photon loss, which include the contributions from the detector inefficiency, the inefficiency of the excitation transfer from the collective atomic mode to the optical mode, and the small decay of the atomic excitation during the storage. (Note that by introducing the detector inefficiency, we have automatically taken into account the imperfection that the detectors cannot distinguish between one and two photons.) With all these losses, the overall efficiency in the entanglement swapping is denoted by η_s. The loss in the entanglement swapping gives contributions to the vacuum coefficient in the connected EME state, since in the presence of loss a single detector click might result from two collective excitations in the ensembles I_1 and I_2, and in this case, the collective modes in the ensembles L and R have to be in a vacuum state. After taking into account the realistic noise, we can specify the success probability and the new vacuum coefficient for the ith entanglement connection by the recursion relations

$$p_i \equiv f_1(c_{i-1}) = \frac{\eta_s\left[1 - \frac{\eta_s}{2(c_{i-1}+1)}\right]}{c_{i-1} + 1}, \tag{8}$$

$$c_i \equiv f_2(c_{i-1}) = 2c_{i-1} + 1 - \eta_s. \tag{9}$$

The coefficient c_0 for the entanglement preparation is typically much smaller than $1 - \eta_s$, so $c_i \approx (2^i - 1)(1 - \eta_s) = (L_i/L_0 - 1)(1 - \eta_s)$, where L_i denotes the communication distance after i entanglement connections. With this expression for the c_i, we can easily evaluate the probability p_i and the communication time T_n for establishing a EME state over the distance $L_n = 2^n L_0$. After the entanglement connection, the fidelity of the EME state also decreases, and after n entanglement connections, the overall fidelity imperfection $\bar{F}_n \sim 2^n \bar{F}_0 \sim (L_n/L_0)\bar{F}_0$. This infidelity $\bar{F}_n$ can be small by simply decreasing the excitation probability p_c, from Eq. (7).

It is important to point out that this entanglement connection scheme also has built-in entanglement purification. This can be understood as follows: each time we connect entanglement, the imperfections of the setup decrease the entanglement fraction $1/(c_i + 1)$ in the EME state. However, the entanglement fraction

decays only linearly with the distance (the number of segments), which is in con-
trast to the exponential decay of the entanglement for the connection schemes
without entanglement purification. The reason for the slow decay is that in each
time of the entanglement connection, we need repeat the protocol only until there
is a detector click. The confirmation of a click removes part of the added vacuum
noise, since a larger vacuum component of the EME state results in more repeti-
tion. The built-in entanglement purification in the connection scheme is essential
for the polynomial scaling law of the communication efficiency.

As in the entanglement generation and connection schemes, the entanglement
application schemes also have built-in entanglement purification which makes
them resilient to practical noise. First, we have seen that the vacuum components
in the EME states are removed from the confirmation of the detector clicks and
thus have no influence on the fidelity of all the application schemes. Second, if
the single-photon detectors and the atom-to-light excitation transitions in the ap-
plication schemes are imperfect with the overall efficiency denoted by η_a, these
imperfections only influence the efficiency to get the detector clicks with the suc-
cess probability now given by $p_a = \eta_a/[2(c_n + 1)^2]$, and have no effects on
the communication fidelity. Finally, we have seen that the phase shifts in the sta-
tionary channels and the small asymmetry of the stationary setup are removed
automatically when we project the EME state to the PME state, and thus have no
influence on the communication fidelity.

As a result of the built-in entanglement purification in each step of the DLCZ
scheme, we can fix the communication fidelity to be nearly perfect, and at the
same time keep the communication time to increase only polynomially with the
distance. Assume that we want to communicate over a distance $L = L_n = 2^n L_0$.
By fixing the overall fidelity imperfection to be a desired small value $\bar{F}$, the en-
tanglement preparation time becomes $T_0 \sim t_\Delta/(\eta_p \bar{F}_0) \sim (L_n/L_0)t_\Delta/(\eta_p \bar{F})$.
For an effective generation of the PME state (6), the total communication time is
$T_{tot} \sim T_n/p_a$, with $T_n \sim T_0/\prod_{i=1}^{n} p_i$. So the total communication time scales
with the distance by

$$T_{tot} \sim 2t_\Delta \left(\frac{L}{L_0}\right)^2 \frac{1}{\eta_p p_a \bar{F} \prod_{i=1}^{n} p_i}, \tag{10}$$

where the success probabilities p_i, p_a for the ith entanglement connection and for
the entanglement application have been specified earlier. Equation (10) confirms
that the communication time T_{tot} increases with the distance L only polynomially,
with the understanding that the number of segments n itself depends logarithmi-
cally on L.

We illustrate this polynomial scaling explicitly in two limiting cases.

- For high efficiency entanglement swapping ($1 - \eta_s \ll 1$), the communication time in Eq. (10) is

$$T_{tot} \sim \tau_C \left(\frac{L}{L_0} \right)^2 e^{L_0/L_{att}}, \tag{11}$$

with the prefactor $\tau_C \equiv 2t_\Delta/(\eta'_p \eta_a \bar{F})$ independent of the segment and the total distances L_0 and L. In this case, the communication time T_{tot} increases quadratically with L.

- For low efficiency entanglement swapping with a significant inefficiency $1 - \eta_s$, the communication time is approximated by

$$T_{tot} \sim \tau_C \left(\frac{L}{L_0} \right)^{\frac{1}{2} \log_2 \frac{L}{L_0} + \log_2(\frac{1}{\eta_s} - 1) + \frac{5}{2}} e^{L_0/L_{att}}, \tag{12}$$

also exhibiting a polynomial increases with L. (More rigorously, this scaling is considered sub-exponential, but there is no practical difference because the polynomial order $\log_2(L/L_0)$ is well bounded from above for any reasonably long distance.) In general, when T_{tot} increases with L/L_0 by an mth-order power law $(L/L_0)^m$, choosing a segment length $L_0 = mL_{att}$ minimizes the net communication time T_{tot}. As a simple estimate of the improvement in the communication efficiency, we assume that the total distance L is about $100L_{att}$, for a choice of the parameter $\eta_s \approx 2/3$, the communication time $T_{tot}/\tau_c \sim 10^6$, using the optimal segment length $L_0 \sim 5.7L_{att}$. This result is a dramatic improvement compared with the direct communication case, where the communication time T_{tot} for getting a PME state increases with the distance L exponentially: $T_{tot} \sim T_0 e^{L/L_{att}}$. For the same distance $L \sim 100L_{att}$, this requires $T_{tot}/T_0 \sim 10^{43}$ for direct communication, which implies that for this example, the DLCZ scheme becomes 10^{37} times more efficient through implementation of the quantum repeater architecture.

2.5. Experimental Quantum Communication with Atomic Ensembles

Remarkable experimental advances in implementing the DLCZ scheme have been reported in recent years (Kuzmich et al., 2003; Van der Wal et al., 2003; Chou et al., 2004, 2005; Matsukevich and Kuzmich, 2004; Blinov et al., 2004; Balic et al., 2005; Chaneliere et al., 2005; Eisaman et al., 2005; Manz et al., 2006; Riedmatten et al., 2006; Matsukevich et al., 2006), targeted to demonstration of scalable quantum communication with atomic ensembles. The first two experiments were reported in 2003 by the Caltech and the Harvard groups (Kuzmich et al., 2003; Van der Wal et al., 2003), where the non-classical correlation between

the symmetric atomic mode S and the signal light mode a was observed. Demonstration of this correlation is fundamental to the entanglement generation scheme in the DLCZ approach, and also shows the collective enhancement effect in the atomic ensemble for the associated level configuration.

In these initial demonstrations, the symmetric atomic mode S is transferred to another photon mode b, and the correlation is actually measured between the photonic modes a and b. The Caltech experiment (Kuzmich et al., 2003) operates in the weak pumping region as assumed in the DLCZ scheme, and it introduces a useful quantity from the Cauchy–Schwarz inequality to characterize the non-classical correlation between the modes a and b (and thus S and a). From the photon counting measurements of these two photonic modes, the self-correlation functions $\tilde{g}_{a,a}$, $\tilde{g}_{b,b}$ and the cross-correlation function $\tilde{g}_{a,b}$ can be defined. For any two classical light fields (as in quantum optics, "classical" here means that the fields can be described with a positive P-representation), these correlations satisfy the so-called Cauchy–Schwarz inequality $[\tilde{g}_{a,b}]^2 \leqslant \tilde{g}_{a,a}\tilde{g}_{b,b}$, while this inequality could be violated for fields with non-classical correlation. So, if one defines a quantity $\eta \equiv [\tilde{g}_{a,b}]^2/(\tilde{g}_{a,a}\tilde{g}_{b,b})$, $\eta > 1$ is a clear experimental signature for non-classical correlation. This quantity η has been measured to be about 1.84 in the first experiment (Kuzmich et al., 2003), and now its value can be pushed above hundreds (Riedmatten et al., 2006; Matsukevich et al., 2006), signaling a much better signal-to-noise ratio. The Cauchy–Schwarz inequality and the associated ratio η is widely used in experiments to characterize noise and quantify entry into the quantum region.

More recently, several experiments have coherently manipulated two separate atomic ensembles (Matsukevich and Kuzmich, 2004; Chou et al., 2005; Chaneliere et al., 2005; Eisaman et al., 2005; Matsukevich et al., 2006). The coherence or entanglement of the two ensembles using the above entanglement generation scheme has been shown (Matsukevich and Kuzmich, 2004; Chou et al., 2005; Matsukevich et al., 2006), and quantum states have been coherently transferred from one ensemble to the other (Chaneliere et al., 2005; Eisaman et al., 2005).

The level configuration investigated in Duan et al. (2001) also provides a new scheme to generate entangled photon pairs, with one photon of the pair able to be stored in the atomic ensemble with a controllable delay time. This ability, together with the projection measurements by the photon counts, have a number of interesting applications for engineering the states of the photon pulses (Chou et al., 2004) and for proof-of-principle demonstration of storage of the single photon pulses (Chaneliere et al., 2005; Eisaman et al., 2005).

In addition to atomic ensembles, various other physical systems have been proposed to replace the atomic ensembles in the DLCZ scheme. For instance, ensembles of electron spins or nuclear spins in quantum dots (or other solid-state systems) can be considered (Childress et al., 2006), given that the electron or

nuclear spins are sufficiently identical (have a small inhomogeneous shift), and exhibit a sufficiently long coherence time.

Single trapped atoms or ions can also replace the atomic ensemble (Duan et al., 2004). In this case, there is of course no collective enhancement effect for the coupling to light, so the entanglement connection efficiency can be significantly reduced. However, for local ions at the same node, the Coulomb interaction can be exploited to perform local quantum gates and entangle different segments of the system. This provides an alternative way for efficient entanglement connections and the construction of quantum repeaters or quantum networks (Duan et al., 2004). The advantage with the trapped ion system is that single ions behave as near-ideal quantum memories, having coherence times far exceeding that of atomic ensembles. Moreover, the ion trap system is a leading candidate for the implementation of quantum computers (Monroe, 2002). In this context, it may be desirable to wire together remotely-located ions through photons, an important step towards distributed quantum computation and the "quantum internet". Along these lines, an initial experiment has been reported in 2004 (Blinov et al., 2004), where entanglement was observed between a single trapped ion qubit and a spontaneous emission photon, therefore demonstrating entanglement between an ideal quantum memory and a flying qubit. Further experiment has confirmed the violation of the Bell inequality corresponding to this entanglement (Moehring et al., 2004). Similar entanglement has also been measured subsequently between a single neutral atom and a photon (Volz et al., 2006).

3. Quantum State Engineering with Realistic Linear Optics

3.1. Linear Optics and Quantum State Engineering

In this section, we review some protocols to generate many-body entangled states with linear optics elements. It is closely related to topics in the previous section in that these schemes are inherently robust to the dominant noise in the corresponding experimental system. For quantum communication, we would like to establish an entangled EPR-like or Bell state over a long distance, and are interested in the scaling of total communication time and the communication distance. For quantum state engineering, we would like to generate more diverse and complex quantum states of many qubits, and are interested in the scaling of total preparation time and the number of qubits.

Linear optics, combined with practical single-photon sources and detectors, has provided a powerful tool to test a number of quantum information protocols (Kwiat et al., 1995; Bouwmeester et al., 1997; Boschi et al., 1998; Pan et al., 2001; Walther et al., 2005). In linear optics implementations of quantum information processing, the post-selection technique of photon detection typically plays a critical role. However, as the system is scaled up,

this post-selection naïvely leads to an exponential scaling of the overall efficiency (or success probability) with the size of the system. A remarkable linear optics quantum computation scheme was proposed by Knill et al. (2001), which in principle can be used to overcome this scaling problem. But the implementation of the KLM scheme requires photon detectors with a very high efficiency, far beyond than the efficiency of the state-of-the-art photon detectors. In the past few years, there have been a number of proposals to improve upon the original linear optics computation scheme (Yoran and Reznik, 2003; Nielsen, 2004; Browne and Rudolph, 2005), some of which employ a graph state approach to quantum computation (Raussendorf and Briegel, 2001; Hein et al., 2006). The threshold efficiency for the photon detectors has also been improved considerably, with the most recent estimate about 99.7% (Dawson et al., 2006) (although it is still significantly beyond the efficiency of practical photon detectors).

We now review quantum state engineering schemes that do not require a high threshold efficiency on the photon detectors. Earlier, it was shown that GHZ types of entangled states can be prepared with linear optical devices and low efficiency photon detectors (Duan, 2002). Recently, this scheme has been extended to generate any "graph" state, which can be used for quantum information protocols and universal quantum computation (Raussendorf and Briegel, 2001; Hein et al., 2006). Moreover, a particular class of entangled states represent by "tree" graphs can be prepared efficiently with photon detectors of *any* efficiency. This approach overcomes the inefficient scaling through the "divide-and-conquer" method, similar to the quantum repeater protocol. While tree graph states have not yet been proven universal for quantum computation (Shi et al., 2006), they can still be used for implementation of a number of other quantum information protocols, including quantum communication, networking, and fundamental test of quantum mechanics (Hein et al., 2006).

In this section, we review this scheme for engineering graph state entanglement following the approach in Bodiya and Duan (**?**). We analyze the effect of a polarization beam splitter (PBS) in the Hilbert subspace post-selected by the photon detections, and show that a single PBS actually represents a powerful gate for generating graph states of arbitrary shapes. This PBS gate is more efficient than other linear optical quantum gates (Knill et al., 2001; Nielsen, 2004; Browne and Rudolph, 2005), not wasting any ancilla photons within each gate operation. Finally, we review a method for scalable generation and detection of many-qubit entangled states represented by tree graph states. Here, by "scalable", we mean the overall efficiency for preparation of a large-scale entanglement with a tree-graph structure scales nearly polynomially with the number of qubits. This efficient scaling persists no matter how small the efficiencies of the photon sources or detectors.

3.2. Preparation of Arbitrary Graph States

We assume to have an imperfect source of entangled photon pairs, which generates states of the following form

$$\rho_s = (1 - \eta_s)\rho_{vac} + \eta_s|\Psi\rangle_{12}\langle\Psi|, \tag{13}$$

where $|\Psi\rangle_{12} = (|HH\rangle_{12} + |VV\rangle_{12})/\sqrt{2}$ represents single photons in two distinct (spatial) modes (1 and 2) entangled through their (internal) polarization states $|H\rangle$ and $|V\rangle$. The state ρ_{vac} represents the vacuum component with zero photons in modes 1 and 2; and η_s is the source efficiency for producing the entangled photon pair. In experiments, the entangled photon source is typically provided through the process of spontaneous parametric down conversion (SPDC), where the source efficiency $\eta_s \ll 1$ (Kwiat et al., 1995; Bouwmeester et al., 1997; Boschi et al., 1998). The pair state of Eq. (13) can also be generated from other experimental setups, such as from decay of a single dipole (which could be a single atom, ion, or a quantum dot) in free space or in a cavity (Blinov et al., 2004), or from decay of an collective excitation in an atomic ensemble (Duan et al., 2001; Chaneliere et al., 2005; Eisaman et al., 2005). In these cases, one mode of the entangled pair is typically represented by a matter qubit (see the previous section), which can be transferred later to a photon qubit after a controllable delay.

Now we show any graph state in the Hilbert subspace post-selected by the photon detection can be generated from the pair states [Eq. (13)] through a series of PBS gates. An n-qubit graph state is defined as the co-eigenstate of n independent stabilizer operators $S_i = X_i \prod_j Z_j$, where i denotes qubit i (each qubit is associated with a vertex of the graph), j runs over all the neighbors of the qubit i, and X_i, Z_i are the Pauli operators σ_x and σ_z for qubit i (Raussendorf and Briegel, 2001; Hein et al., 2006). In a graph, the qubits i and j are called neighbors if they are connected with an edge. The graph state reduces to a cluster state if the corresponding graph is a periodic lattice (Hein et al., 2006).

To show construction of the graph states, first we must consider the effect of a PBS in the subspace post-selected by the photon detection. For linear optics quantum information, all the photon modes are measured eventually in an appropriate polarization basis by a single-photon detector. We are interested only in the measurement outcomes with one photon registered from each mode (its polarization can be arbitrary). So, by this final measurement, one post-selects a Hilbert subspace, which we denote as S. We need only determine the state evolution in this "physical" subspace S, as the state component outside S has no influence on the final measurement of the polarization qubits.

A PBS lets the photon through if it is in the H polarization state, and reflects it if it is in the V polarization state. After the PBS, photons from the two incoming modes therefore emerge along different modes if and only if both photons have the same polarization (either HH or VV). Otherwise, the photons emerge from the

PBS in the same spatial mode with the other mode in the vacuum state—outside of the "physical" subspace S. So, within the subspace S, the effect of a PBS is to perform a projection on the input state, described by the projector

$$P = |HH\rangle_{12}\langle HH| + |VV\rangle_{12}\langle VV|. \tag{14}$$

This projection is equivalent to a measurement of the operator $Z_1 Z_2$ on the two input qubits 1 and 2, with the final state undisturbed only for measurement outcome "+1" ($|HH\rangle_{12}$ and $|VV\rangle_{12}$ are eigenstates of $Z_1 Z_2$ with an eigenvalue "+1"). So in the physical subspace S, a single PBS performs an effective $Z_1 Z_2$ measurement gate with a success probability of $1/2$ (the probability to stay in the "physical" space S after the PBS).

We start with two entangled pairs 1, 2 and 3, 4, each pair described by the state of Eq. (13). In the subspace S, the effective state is then given by $|\Psi\rangle_{12}$, which can be transferred to a two-bit graph state with a straightforward Hadamard gate on one of the qubits. Consequently, for the pairs 1, 2 and 3, 4, we can assume them to have the stabilizer operators $X_1 Z_2$, $X_2 Z_1$ and $X_3 Z_4$, $X_4 Z_3$, respectively. If the qubits 2 and 3 pass through a PBS, the effective output state in the subspace S is then stabilized by the operators $Z_2 Z_3$, $X_2 X_3 Z_1 Z_4$, $X_2 Z_1$, and $X_4 Z_3$. (The second operator is just a product of the previous stabilizers $X_2 Z_1$ and $X_3 Z_4$, and it remains unchanged after the PBS because it commutes with the effective measurement gate $Z_2 Z_3$.) With a straightforward Hadamard gate $X_3 \leftrightarrow Z_3$, implemented with a half-wave plate, the above four stabilizers transform to the standard stabilizers for the 4-bit star-shape graph state as shown in Fig. 5.

For convenience, we label the combination of the PBS and single-bit Hadamard operation the PBS gate (see Fig. 5). An extension of the above construction yields the following important result: the PBS gate always joins two pieces of graphs, independent of the shapes of the initial pieces. This result can be proven generally as follows. We start with two pieces of graph states G_1 and G_2, with n and m qubits, respectively. The stabilizers associated with the qubits i_1 and i_2 are given by $S_{i_l} = X_{i_l} \prod_{j_l \in N(i_l)} Z_{j_l}$ ($l = 1, 2$), where i_l is an arbitrary vertex of the graph G_l and $N(i_l)$ denotes all the neighbors of the qubit i_l in the graph G_l. After a PBS gate on the qubits i_1 and i_2, the stabilizers S_{i_2} and S_{i_1} are replaced by

$$S'_{i_2} = X_{i_2} Z_{i_1} \quad \text{and} \quad S'_{i_1} = X_{i_1} Z_{i_2} \prod_{j_1 \in N(i_1)} Z_{j_1} \prod_{j_2 \in N(i_2)} Z_{j_2}.$$

All the other stabilizers of the initial graphs G_1 and G_2 remain unchanged after the gate. One can immediately see that the effective output state of the PBS gate is still a graph state which combines the two initial graphs G_1 and G_2, with i_2 attached to i_1, and i_1 attached to i_2 and all their initial neighbors in the graphs G_1 and G_2 [see Fig. 5(c)].

Given the above result, it becomes possible to construct graph states of any shape with a series of PBS gates. In Figs. 5 and 6, we illustrate this by constructing
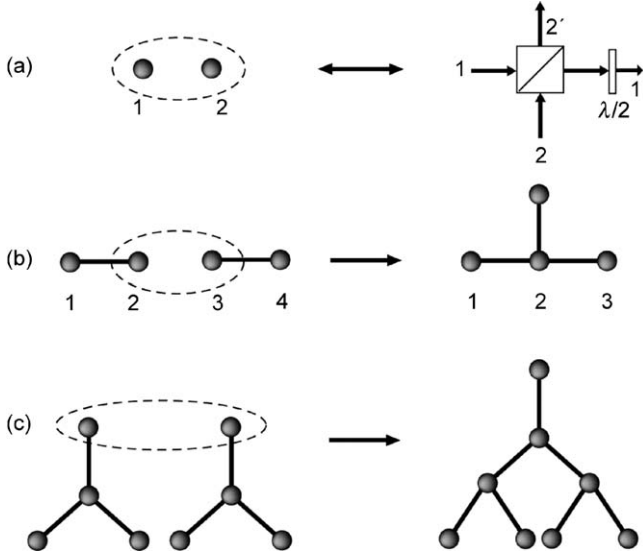
FIG. 5. (a) Representation of the PBS gate, which consists of a polarization beam splitter and a half-wave plate (for a Hadamard operation on one mode). (b) and (c): Illustration in which PBS gates generate tree graph states. It is obvious that tree graphs of any shapes can be generated with this method (see Bodiya and Duan, **?**).
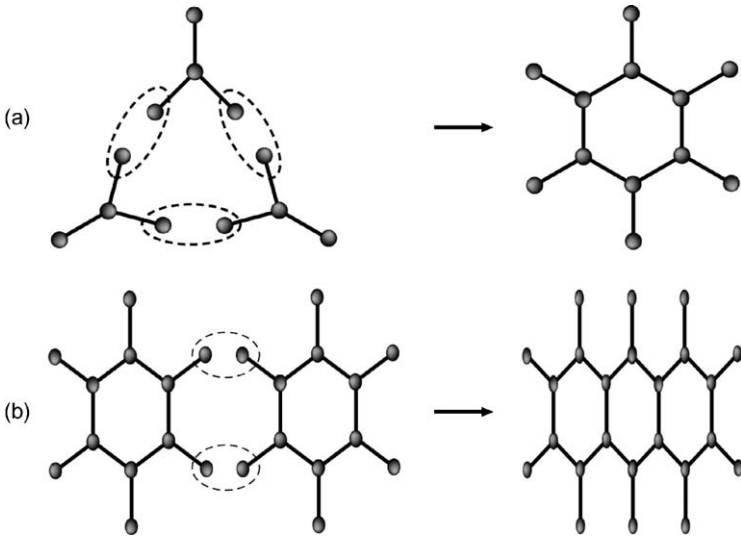

FIG. 6. (a) and (b): Illustration of using the PBS gates to generate 2-dimensional graphs states (see Bodiya and Duan, **?**).

graph states representing a tree graph and a two-dimensional graph with many loops. This construction method is efficient, as no photons are wasted during the state preparation. Starting with n entangled pairs, we can build graph states of $2n$ qubits with various shapes.

3.3. Efficient Generation and Scaling of Tree Graph States

If we assume both the photon sources and detectors have large inefficiencies, we still have inefficient (exponential) scaling for construction of large-scale graph states even with the above PBS gate. In order to generate an n-qubit entangled graph-state, we must consume $n/2$ imperfect entangled pairs represented by the state [Eq. (13)] and detect n photon modes at the end. So, there is a factor of $\eta_d^n \eta_s^{n/2}$ in the preparation efficiency, where η_d is the efficiency for each individual detector. If we require $m \leqslant n/2$ PBS gates to arrive at such a graph state, there is an additional factor of $(1/2)^m$ in the preparation efficiency associated with the intrinsic gate success probability to stay in the subspace S. In the case of a small source efficiency η_s (such as for the SPDC experiments), the preparation efficiency degrades rapidly with the size of the state, limiting the current implementation to only a few qubits (Kwiat et al., 1995; Bouwmeester et al., 1997; Boschi et al., 1998; Pan et al., 2001; Walther et al., 2005). In the following, we show that an important subclass of graph states—"tree" states—can be prepared and detected efficiently with a number of operations that scales polynomially in the state size. As the name implies, tree states are defined as graph states where any two vertices are connected by exactly one path.

This efficient scaling method is based on a combination of the ideas of the divide-and-conquer (quantum repeater) protocol and the post-selection measurements. We note that for applications of graph states in linear optics quantum information, each photon mode needs to be eventually measured in some polarization basis. This suggests that the whole protocol can be divided into two logical steps: the graph state preparation and the application measurement. For the second step, measurement of each photon mode has a finite failure probability, where instead of getting the photon's polarization, one does not register any photon. To boost the efficiency of the whole protocol, it is better to sort out and discard these failure events as soon as possible. In this spirit, we can try to apply the application measurements on some individual qubits before we finish the first logic step of the graph-state preparation. We measure the qubits as soon as we do not need to apply the PBS gates on those qubits any more. When we register a failure event, we immediately discard the qubits that are influenced by the failure event, and restart the state preparation for that segment.
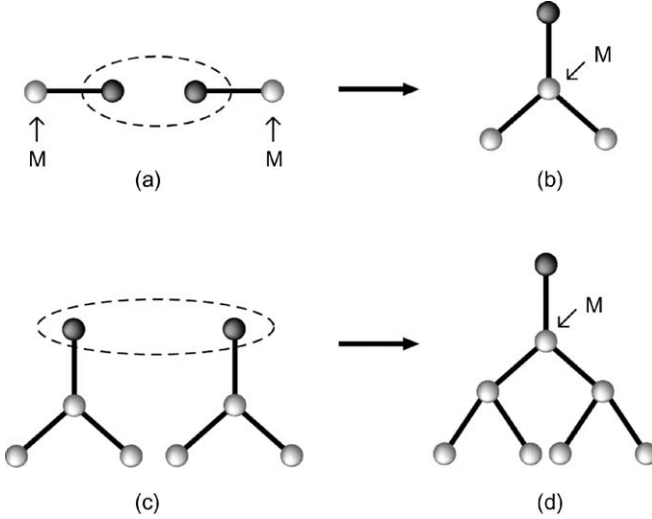
FIG. 7. Efficient construction of tree-graph states. White circles represent qubits that have been measured in appropriate polarization bases, and black circles represent the connection qubits (unmeasured) that enable the next-step connection. (a) Before connection of the two center qubits, the two edge qubits have been measured. (b) After connection, we immediately measure one of the connection qubits, and leave the other one for the next step connection as shown in (c). (c) and (d): Repetition of the process of connection/measurement for construction of larger graphs (see Bodiya and Duan, **?**).

Figure 7 illustrates how such an idea works for preparation and detection of a tree-graph state. We start with two pairs $(1, 2)$ and $(3, 4)$, with the pair state described by Eq. (13). As we do not need to apply the PBS gates on the qubits 1 and 4 in the following steps, we immediately measure them in the polarization basis chosen according to the targeted application protocol. The measurement on the qubit 1 (or 4) succeeds with a probability $p_0 = \eta_s \eta_d$, and upon success, the vacuum component in the imperfect state [Eq. (13)] is eliminated. If we fail in the measurement of qubit 1, we simply prepare the state for the pair $(1, 2)$ once again, with the pair $(3, 4)$ intact. After an average number of trials $\sim 1/p_0$, we succeed in entangling the qubit pair $(1, 2)$ and eliminating their vacuum component. Simultaneously, we can do the same to qubit pair $(3, 4)$ after $\sim 1/p_0$ trials. Then, we continue with the connection of the qubits 2 and 3 through a PBS gate, and after the connection, we immediately measure the qubit 2 as we only need keep qubit 3 for the next step of connection. This process is continued until we get an effective tree-graph state with a desired number of qubits, as outlined in the figure.

To determine the overall efficiency for generation of this graph-state entanglement, we specify recursion relations for each step of connection. For each connection, the number of qubits is doubled. For the mth connection, the effective

state before connection can be written as $\rho_{2n}^a = \rho_n \otimes \rho_n$, where ρ_n is the state of a segment which has $n = 2^m$ qubits. The segment state can be expressed as $\rho_n = a_{m-1}\rho_g + (1 - a_{m-1})\rho_{vac}$, where ρ_g denotes the effective n-qubit tree graph state and ρ_{vac} represents the vacuum component where the connection qubit of the graph is in the vacuum state. For the 1st connection [of pairs $(1, 2)$ with $(3, 4)$], $a_0 = 1$ because the vacuum component has been eliminated by the measurement on qubits 1 and 4. After the mth connection, we immediately measure one of the two connection qubits (the other one is kept as the connection qubit for the next step). The success probability for this measurement is given by

$$p_m = \eta_d \left[\frac{a_{m-1}^2}{2} + \frac{a_{m-1}^2(2 - \eta_d)}{4} + a_{m-1}(1 - a_{m-1}) \right], \tag{15}$$

where we have assumed the detector cannot distinguish the single-photon and two-photon counts, as is the case in practice. Upon a success of this measurement, the effective state for the $2n$ qubits becomes $\rho_{2n} = a_m\rho_g + (1 - a_m)\rho_{vac}$, where ρ_g and ρ_{vac} have the same meaning as before except that they are for $2n$ qubits now, and the coefficient a_m is given by the recursion relation $a_m = 2a_{m-1}/(4 - \eta_d a_{m-1})$. Together with $a_0 = 1$, this recursion relation yields

$$a_m = \frac{2}{2^m(2 - \eta_d) + \eta_d}. \tag{16}$$

To prepare and confirm an $n = 2^m$ qubit entanglement represented by the tree graph state, the overall efficiency of the scheme can be characterized by the total preparation time T. From the above recursion relations, we find that

$$T = \frac{t_0}{\eta_d a_{m-1}} \prod_{i=0}^{m-1} \frac{1}{p_i}$$

$$\approx \left(\frac{t_0}{\eta_s \eta_d} \right) n^{\frac{1}{2}(\log_2 n - 1) + \log_2\left(\frac{1}{\eta_d} - \frac{1}{2}\right)}, \tag{17}$$

where the approximation is valid when $\eta_d/2 \ll n$, and we have assumed that the two segments of graphs states before each connection can be prepared in parallel simultaneously. Note that overall preparation time scales linearly with t_0, the time to generate an imperfect pair [Eq. (13)]. In the case of SPDC photon sources, this is roughly the inverse of the pulse repetition rate in these systems (Kwiat et al., 1995; Bouwmeester et al., 1997; Boschi et al., 1998; Pan et al., 2001; Walther et al., 2005). We find that T also scales nearly polynomially with the size n of the final graph state, and such a scaling holds for any source efficiency η_s and detector efficiency η_d.

The following example illustrates the dramatic improvement in scaling compared with conventional (sequential) entanglement techniques. If we take the source efficiency $\eta_s \sim 1\%$ and the detector efficiency $\eta_d \sim 33\%$, we find

$T/t_0 \sim 3.0 \times 10^7$ (3.6×10^4) for preparation of a graph state of 32 (8) qubits. If the pulse repetition rate is 80 MHz, typical for mode-locked laser sources (Kwiat et al., 1995; Bouwmeester et al., 1997), the total preparation time is $T \sim 0.37$ s (0.45 ms), which is still reasonable. If we do not use this divide-and-conquer technique, the total time required to produce a 32-qubit graph state is $T/t_0 = \eta_s^{-32/2}\eta_d^{-32}2^{32/2-1} \sim 10^{52}$, or $T \sim 10^{44}$ s.

We point out that a very recent experiment has reported demonstration of six photon graph states (Lu et al., 2006), using exactly the above PBS gate.

4. Quantum Computation through Probabilistic Atom–Photon Operations

4.1. Robust Probabilistic Gates

In this section, we review some schemes and experimental progress towards scalable quantum computing with probabilistic type of gates on atoms or ions. In the previous two sections, we have reviewed methods to achieve inherently robust quantum communication and state engineering. Similarly, we also strive to achieve inherent fault tolerance to the dominant experimental noise in quantum computing applications. This is the main motivation for using probabilistic quantum gates, where the dominant noise merely contributes to the gate inefficiency and does not necessarily lead to infidelity of quantum gates. With noise, the entangling gate succeeds with a finite (even small) probability, but we know with near-certainty when it does succeed. It becomes much easier to correct these probabilistic type of errors. We show that universal quantum computers can be constructed efficiently even if the entangling gate only succeeds with an arbitrarily small probability. Thus, through design of probabilistic gates, we can tolerate the dominant experimental noise at very high levels.

The probabilistic gate covered in this section is different from the probabilistic entangling operations and the post-selected PBS gate that we have reviewed in the last two sections. Although all of these operations share the property of inherent insensitivity to noise, only the probabilistic gate can lead to scalable quantum computation. Compared with deterministic gates, the additional overhead in resources (such as the number of qubit manipulations) for quantum computing with probabilistic gates scales only polynomially with both the size of the computation and the inverse of the gate success probability.

In the next section, following the approach in Duan et al. (2006), we review a scheme for probabilistic gates on remote ions or atoms through interference of photonic qubits stored in the frequency (color) of the photons. There are other proposals for implementation of probabilistic gates using atomic qubits (Barrett and

Kok, 2005; Duan et al., 2005; Lim et al., 2006). However, the scheme reviewed here is considerably simpler with regard to experimental requirements:

- The gate operates on atoms in free space without the need for optical cavities, and uses ideal atomic ground state hyperfine energy levels as matter qubits.
- Optical *frequency* qubits are used to connect and entangle matter qubits at distant locations. The two states comprising this optical qubit have the same polarization, but differ in frequency by the atomic hyperfine splitting (typically in the microwave region). These closely-spaced frequency components have basically zero dispersion in typical optical paths, thus this optical qubit is highly insensitive to phase jitter inherent in optical interferometers.
- The gate scheme does not require interferometric stabilization of the optical path lengths to near or within an optical wavelength.
- The motion of the atomic qubits need not be confined to within an optical wavelength (the Lamb–Dicke regime).

After a review of this probabilistic gate scheme, we then show how efficient universal quantum computation can be accomplished with probabilistic entangling quantum gates, following the approach in Duan and Raussendorf (2005). Finally, we review recent experimental progress towards demonstration of the probabilistic quantum gates in the trapped ion system (Madsen et al., 2006; Maunz et al., 2006).

4.2. PROBABILISTIC GATES FROM FREE-SPACE ATOM–PHOTON COUPLING

The scheme for probabilistic gates between remote atoms is illustrated in Fig. 8. The qubit is represented by two $S_{1/2}$ ground state hyperfine levels of an alkali-like atom (ion), with $|0\rangle \equiv |F, m = 0\rangle$, and $|1\rangle \equiv |F + 1, m = 0\rangle$. These "clock" states are particularly insensitive to stray magnetic fields. In the figure, for simplicity, we take $F = 0$, which is the case for ions such as $^{111}\text{Cd}^+$, but the scheme works for any value of F. To perform a probabilistic gate on two remote atoms 1 and 2, we first excite both of the atoms to the $P_{1/2}$ excited electronic state with a π-polarized ultrafast laser pulse. We assume the laser has a bandwidth which is larger than the ground state hyperfine splitting (14 GHz for $^{111}\text{Cd}^+$), but smaller than the fine structure splitting between $P_{1/2}$ and $P_{3/2}$ (74 THz for $^{111}\text{Cd}^+$). Typical picosecond pulses used in experiments (bandwidth ~ 500 GHz) satisfy these requirements (Madsen et al., 2006). Under the above condition, we can assume the pulse drives only the $D1$ transition from the ground state $S_{1/2}$ to the excited state $P_{1/2}$. [For any atoms with nuclear spin $I = 1/2$ such as $^{111}\text{Cd}^+$, one can also drive the $D2$ line $S_{1/2} \to P_{3/2}$, where the two corresponding hyperfine transitions are given by $|F, m = 0\rangle \to |F', m = 0\rangle$ and $|F + 1, m = 0\rangle \to |F' + 1, m = 0\rangle$ with $F' = F + 1$, see Madsen et al. (2006).] Due
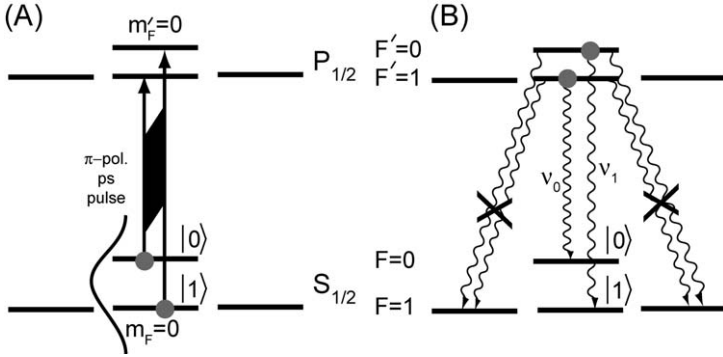
FIG. 8. The atomic level configuration and the laser excitation scheme. (A) An ultrafast laser pulse transfers the atomic qubit state from the ground levels to the excited levels. (B) The atom decays back to the ground levels, with the frequency of the spontaneously emitted photon correlated with the atomic qubit state (marked as the signal mode ν_0 and ν_1 in the figure). The photon from the $\sigma^{\pm}$ decay channels is filtered through polarization selection (see Duan et al., 2006).

to dipole selection rules, for a π-polarized pulse, only the hyperfine transitions $|F, m = 0\rangle \rightarrow |F' + 1, m = 0\rangle$ and $|F + 1, m = 0\rangle \rightarrow |F', m = 0\rangle$ are allowed, where the upper hyperfine spin $F' = F$. Thanks to the selection rules, each qubit state is transferred to a unique excited hyperfine level after the pulsed laser excitation. This point is critical for successful gate operation.

After this laser excitation, the atoms eventually decay back to their ground $S_{1/2}$ states. There are several decay channels, denoted as π or $\sigma^{\pm}$ in Fig. 8. The spontaneous emission photons from the π and the $\sigma^{\pm}$ decay channels have orthogonal polarizations along the observation direction. We can distinguish them and can block any photon from the $\sigma^{\pm}$ decay channels through a polarization filter. We then consider the π decay channels. In this case, the excited levels $|F' + 1, m = 0\rangle$ and $|F', m = 0\rangle$ can only decay back to the ground states $|F, m = 0\rangle$ and $|F + 1, m = 0\rangle$, respectively. While photons from these two decay channels have the same polarization, they have slightly different frequencies. The frequency difference is given by $\Delta_{HF}^{S} + \Delta_{HF}^{P}$, the sum of the hyperfine splittings of the ground $S_{1/2}$ and excited $P_{1/2}$ states. This frequency difference is typically much larger than the natural linewidth of the excited level. For instance, for ^{133}Cs atoms or ^{111}Cd^{+} ions, the hyperfine splitting is about 9 GHz (14 GHz), while the natural linewidth of the excited level (the inverse of the lifetime) is around 5 MHz (60 MHz). In both cases, the condition is well satisfied. So the corresponding photons from the two π-decay channels are well resolved in frequency. This defines two frequency modes for the emitted photon field, and we call them ν_0 and ν_1 modes, respectively. If the atom is initially in the qubit state $|\Psi_a\rangle = c_0|0\rangle + c_1|1\rangle$, then after this excitation-decay process the atom–photon
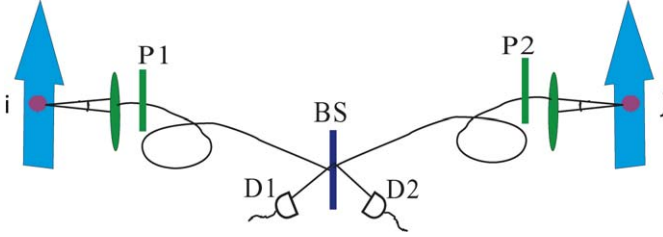
system evolves to an entangled state

$$|\Psi_{ap}\rangle = c_0|0\rangle|v_0\rangle + c_1|1\rangle|v_1\rangle \tag{18}$$

if we only collect the photon from the π decay channels, where $|v_0\rangle$ and $|v_1\rangle$ represent a single photon state in the frequency modes v_0 and v_1, respectively. This result is somewhat similar to the experiment of the atom–photon entanglement (Blinov et al., 2004), but there are important differences. First, the final state $|\Psi_{ap}\rangle$ keeps track of the information c_0, c_1 of the initial qubit state. Thus, the scheme here is not just an entangling protocol, but is instead an entangling *gate* with the final quantum state depending on the initial state. As we see later, this type of gate can form the basis for scalable quantum computation, and is therefore more powerful than merely an entangling operation. Second, the spontaneous emission photon with either frequency v_0 or v_1 has the same spatial mode, so good spatial mode-matching of this photonic qubit is possible even if we increase the solid angle of collection. In the previous entangling protocol (Duan et al., 2004; Blinov et al., 2004), the quantum information is carried by different polarization modes of the photon, which have different spatial emission patterns. This requires small collection solid angles in order to both maintain orthogonality and ensure adequate spatial matching of the photonic qubit states.

To perform a gate on two remote atoms, the spontaneous emission photons from the decay channels in each atom are collected in a certain solid angle, and directed onto a beam splitter for interference (see Fig. 9). The output of the beam splitter is measured by two single-photon detectors. We keep the resulting outcome atomic state only when we register a photon from each detector. In this case, what we have performed is a "measurement gate" on the atoms 1 and 2. It corresponds to a quantum non-demolition measurement of the operator $Z_1 Z_2$, where Z_i (or X_i) stands for the z (or x) component of the Pauli matrix associated with atomic qubit i. After the coincidence measurement of photons on both detectors, the atomic state is projected to the eigenspace of $Z_1 Z_2$ with -1 eigenvalue. To see this, we note that before the measurement, the state of both atom–photon systems can be written as $|\Psi_{ap}\rangle_1 \otimes |\Psi_{ap}\rangle_2$, where $|\Psi_{ap}\rangle_1$ has the form of Eq. (14), and $|\Psi_{ap}\rangle_2$ can be written as $|\Psi_{ap}\rangle_2 = d_0|0\rangle_2|v_0\rangle_2 + d_1|1\rangle_2|v_1\rangle_2$. To register a photon from each detector, the two photons before the beam splitter need to go to different sides, which means they should be in the anti-symmetric component $|\Phi_{AS}\rangle = (|v_0\rangle_1|v_1\rangle_2 - |v_1\rangle_1|v_0\rangle_2)/\sqrt{2}$ (for photons in the symmetric states, they always go to the same detector). So, given that the photons take separate paths after the beam splitter, the state of the atoms 1, 2 is given by the projection

$$\begin{aligned}
|\Psi_{12}\rangle &\propto \langle\Phi_{AS}||\Psi_{ap}\rangle_1 \otimes |\Psi_{ap}\rangle_2 \\
&\propto c_0 d_1|0\rangle_1|1\rangle_2 - c_1 d_0|1\rangle_1|0\rangle_2 \\
&\propto Z_1(I - Z_1 Z_2)|\Psi_a\rangle_1 \otimes |\Psi_a\rangle_2, \tag{19}
\end{aligned}$$

FIG. 9. The ZZ measurement gate on the atoms i and j. The spontaneous emission photons from the π decay channels of these two atoms are collected, interfered at the beam splitter (*BS*), and then detected by two single-photon detectors (D_1 and D_2). If each detector registers a photon, the atomic state is projected onto the eigenspace of the $Z_i Z_j$ operator (see Duan et al., 2006).

where $I - Z_1 Z_2$ is the corresponding projector, and Z_1 is a trivial additional single-bit gate on atom 1 which we neglect in the following. This measurement gate, of course, only succeeds with a finite probability. The overall success probability is given by $p_s = \eta_d^2 \eta_c^2 \eta_b^2/4$, where η_d is the quantum efficiency of each detector, η_c is the photon collection efficiency (proportional to the solid angle), and η_b is the branching ratio for the atom to decay along the π channel. We have an additional factor of $1/4$ in p_s describing the average probability for the two spontaneous emission photons to go to different detectors (averaged over all the possible initial atomic states). In the above contributions to the success probability, the collection efficiency is typically the smallest and thus dominates the overall efficiency. That is why it is important to increase the collection solid angle as much as possible. Alternatively, one can also increase this efficiency with the use of optical cavities surrounding the atoms (McKeever et al., 2003). The overall success probability p_s is typically small. For instance, for a $^{111}\text{Cd}^+$ ion decaying from the $P_{3/2}$ state, the branching ratio into the π-channel $\eta_b = 2/3$, the photon collection efficiency $\eta_c \sim 2\%$ in free space (Blinov et al., 2004), and the detector efficiency $\eta_d \sim 20\%$. This leads to an overall success probability $p_s \sim 2 \times 10^{-6}$. If the collection efficiency is increased by a factor of 10 with a larger collection solid angle or with a surrounding cavity (not necessarily high-finesse), the success probability will be significantly increased with a factor of 100.

The above measurement gate is robust to noise. We do not require that the atoms be localized to the Lamb–Dicke limit. In general, atomic motion occurs with a time scale of the trap frequency ν_t, typically much smaller than the decay rate γ of the excited atomic level. Thus, for each spontaneous emission pulse, we can safely assume the atom to be in a fixed but random position $\mathbf{r}$. In this case, both of the frequency components $|\nu_0\rangle$ and $|\nu_1\rangle$ will acquire the same random phase factor proportional to $e^{i\mathbf{k}\cdot\mathbf{r}}$, where $\mathbf{k}$ is the wave vector associated with the spontaneous emission photon. This overall phase therefore has no effect on the resultant measurement gate as shown in Eq. (19). If we take into account the motion

of the atom within the pulse duration, the pulse from this moving atom also has a slight Doppler shift $\delta\omega = \mathbf{k} \cdot \mathbf{v} \sim |\mathbf{k}| v_t l_s$ in its frequency, where $\mathbf{v}$ is the random atom velocity at that moment, and l_s is the characteristic length scale for the atom oscillation. We need this random Doppler shift to be significantly smaller than the bandwidth of the pulse in order to have a good shape matching of the spontaneous emission pulses from different atoms. So, there is a further requirement $|\mathbf{k}| v_t l_s \ll \gamma$, which is consistent with the assumption $v_t \ll \gamma$. Finally, this gate is also very insensitive to the birefringence and the phase drift in the optical interferometer. Both of the components $|v_0\rangle$ and $|v_1\rangle$ have the same polarization, and they are very close in frequency. So, they essentially experience the same noisy phase shift under fluctuation of the optical path length, again canceling.

4.3. Scalable Quantum Computation with Probabilistic Gates

In the previous section, we have shown how to perform probabilistic entangling gates on remote atoms. Such gates only succeed with a small probability, but they are very robust to noise. Naively, if the entangling gates only succeed with a certain probability p, one cannot have efficient computation as the overall success probability (efficiency) scales down exponentially as p^n with the number n of gates. However, in this section we review a method which shows that efficient quantum computation can be constructed with the required computational overhead (such as the computation time or the repetition number of the entangling gates) scaling up slowly (polynomially) with both n and $1/p$. We will follow the approach in Duan and Raussendorf (2005). (Another method was proposed in Barrett and Kok (2005), which applies to a more restricted noise model, where one assumes that the qubits are subject only to Z type of errors when the gate fails. The implementation scheme we reviewed in the previous section does not satisfy this restriction.) The demonstration of this result combines the ideas from the divide-and-conquer method used in the DLCZ scheme (Duan et al., 2001), the cluster state approach to quantum computation (Raussendorf and Briegel, 2001), and the repetitive error correction important for construction of the two-dimensional clusters.

To be more specific, we assume that one can reliably perform the above ZZ measurement gates with a small success probability p. We neglect the noise for all the single-bit operations, which is well justified for typical atomic or optical experiments. Then, to realize efficient quantum computation, our task reduces to how to efficiently construct large scale two-dimensional (2D) cluster states, as 2D clusters, combined with free single-bit operations, realize universal quantum computation. Our basic steps are: first we show how to efficiently prepare a 1D cluster state from the probabilistic ZZ gates using the divide-and-conquer method, then we give a construction to efficiently generate 2D cluster states from 1D chains.
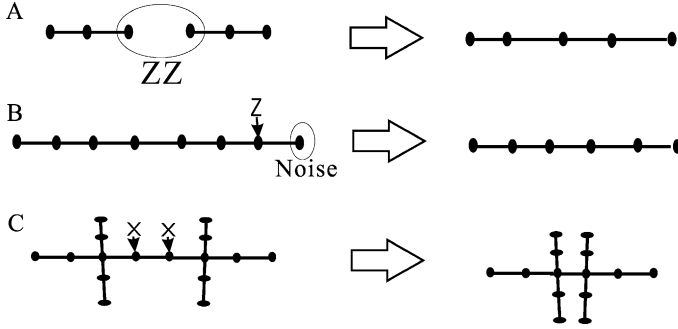
FIG. 10. Illustration of the three properties of the cluster states which are important for our construction of such states with the probabilistic entangling gates: (A) extend cluster states with ZZ measurement gates; (B) recover cluster states by removing bad qubits; (C) shrink cluster states for more complicated links (see Duan and Raussendorf, 2005).

With respect to a given lattice geometry, the cluster state is defined as co-eigenstates of all the operators $A_i = X_i \prod_j Z_j$, where i denotes an arbitrary lattice site and j runs over all the nearest neighbors of the site i. The X_i and Z_j denote respectively the Pauli spin and phase flip operators on the qubits at the sites i, j. In our construction of lattice cluster states with probabilistic ZZ gates, we will make use of the following properties of the ZZ gate or the cluster states: (1) If one starts with two qubits (atoms) in the co-eigenstate of X_1 and X_2 (a product state), the final state after a ZZ measurement is projected to a co-eigenstate of the stabilizer operators $Z_1 Z_2$ and $X_1 X_2$, which is equivalent to the two-qubit cluster state under single-bit rotations (Barrett and Kok, 2005); (2) Assume that one has prepared two 1D cluster chains, each of n qubits. The stabilizer operators for the boundary qubits n and $n + 1$ of the two chains are denoted by $X_n Z_{n-1}$ and $X_{n+1} Z_{n+2}$, respectively. A ZZ measurement of these two boundary qubits generates the new stabilizer operators $Z_n Z_{n+1}$ and $X_n X_{n+1} Z_{n-1} Z_{n+2}$. This operation actually connects the two chains into a cluster state of $2n - 1$ qubits (the central qubits n and $n + 1$ together represent one logic qubit with the encoded $X_L = X_n X_{n+1}$ and $Z_L = Z_n$ or Z_{n+1}. One can also measure the single-bit operator X_{n+1} to reduce the encode operators X_L and Z_L to X_n and Z_n); (3) If we destroy the state of an end qubit of an n-qubit cluster chain, for instance, through an unsuccessful attempt of the ZZ gate, we can remove this bad qubit by performing a Z measurement on its neighboring qubit, and recover a cluster state of $n - 2$ qubits. (4) We can shrink a cluster state by performing X measurements on all the connecting qubits. The last three properties of the cluster states, illustrated in Fig. 10, can be conveniently explained from their above definition (Hein et al., 2006).

If we have generated two sufficiently long cluster chains each of n_0 qubits, we can just try to connect them through a probabilistic ZZ gate. If this attempt fails, through the property (ii), we can recover two $(n_0 - 2)$-qubit cluster chains through a Z measurement, and try to connect them again. As one continues with this process, the average number of qubits in the connected chain is then given by

$$n_1 = \sum_{i=0}^{n_0/2} (2n_0 - 1 - 4i)p(1-p)^i \simeq 2n_0 - 1 - 4(1-p)/p,$$

where the last approximation is valid when $e^{-n_0 p/2} \ll 1$. As a result the average chain length goes up if $n_0 > n_c \equiv 4(1-p)/p + 1$. We can iterate these connections to see how the computation overhead scales with the qubit number n. We measure the computation overhead in terms of the total computation time and the total number of attempts for the ZZ gates. For the rth ($r \geqslant 1$) round of successful connections, the chain length n_r, the total preparation time T_r, and the total number of attempts M_r scale in a manner that can be obtained from the recursion relations

$$n_r = 2n_{r-1} - n_c, \quad T_r = T_{r-1} + t_a/p, \quad \text{and} \quad M_r = 2M_{r-1} + 1/p,$$

respectively. In writing the recursion relation for T_r, we have assumed that two cluster chains for each connection are prepared in parallel, and we neglect the time for single-bit operations (t_a denotes the time for each attempt of the ZZ gate). From the above recursion relations, we conclude that if we can prepare cluster chains of n_0 ($n_0 > n_c$) qubits in time T_0 with M_0 attempts of the probabilistic gates, for a large cluster state, the preparation time T and the number of attempts M scale with the chain length n as

$$T(n) = T_0 + (t_a/p) \log_2\big[(n - n_c)/(n_0 - n_c)\big], \quad \text{and}$$
$$M(n) = (M_0 + 1/p)(n - n_c)/(n_0 - n_c) - 1/p.$$

In the above, we have shown that if one can prepare cluster chains longer than some critical length n_c, one can generate large scale 1D cluster states very efficiently. The problem then reduces to how to efficiently prepare cluster chains up to the critical length n_c. If one wants to prepare an n-qubit cluster chain, we propose to use a repeater protocol which divides the task into $m = \log_2 n$ steps: for the ith ($i = 1, 2, \ldots, m$) step we attempt to build a 2^i-bit cluster state by connecting two 2^{i-1}-bit cluster chains through a probabilistic ZZ gate. If such an attempt fails, we discard all the qubits and restart from the beginning. For the ith step, the recursion relations for the preparation time T_i and the number of attempts M_i are given by $T_i = (1/p)(T_{i-1} + t_a)$ and $M_i = (1/p)(2M_{i-1} + 1)$, which, together with $T_1 = t_a/p$ and $M_1 = 1/p$, give the scaling rules $T(n) \simeq t_a(1/p)^{\log_2 n}$ and $M(n) \simeq (2/p)^{\log_2 n}/2$. The cost is more significant, but it is still a polynomial function of n. To construct a n-qubit cluster chain, in total we need $n - 1$

successful ZZ gates. In a direct protocol, we need all these attempts succeed simultaneously, which gives the scaling $T(n) \propto M(n) \propto (1/p)^{n-1}$. By dividing the task into a series of independent pieces, we improve the scaling with n from exponential to polynomial (for $n \leqslant n_c$).

To generate a cluster chain of a length $n > n_c$, we simply combine the above two protocols. First, we use the repeater protocol to generate n_0-qubit chains with $n_0 > n_c$. Then it is straightforward to use the connect-and-repair protocol to further increase its length. For instance, with $n_0 = n_c + 1$ (which is a reasonable close-to-optimal choice), the overall scaling rules for T and M are (for $n > n_c$),

$$T(n) \simeq t_a (1/p)^{\log_2(n_c+1)} + (t_a/p) \log_2(n - n_c), \tag{20}$$

$$M(n) \simeq (2/p)^{\log_2(n_c+1)}(n - n_c)/2. \tag{21}$$

As the critical length is $n_c \simeq 4/p$, T and M in our protocol scale with $1/p$ as $(1/p)^{\log_2(4/p)}$, which is much more efficient than the super-exponential scaling $(1/p)^{4/p}$ in the previous work.

We have shown that for any success probability p of the probabilistic entangling gate, 1D cluster states of arbitrary length can be created efficiently. For universal quantum computation, however, such 1D cluster states are not sufficient. They need to be first connected and transformed into 2D cluster states (for instance, with a square lattice geometry). It is not obvious that such a connection can be done *efficiently*. First, in the connect-and-repair protocol, when an attempt fails, we need to remove the end qubits and all of their neighbors. This means that in a 2D geometry, the lattice shrinks much faster to an irregular shape in the events of failure. Furthermore, a more important obstacle is that we need to connect many more boundary qubits if we want to join two 2D cluster states. For instance, for a square lattice of n qubits, the number of boundary qubits scales as $\sqrt{n}$ (which is distinct from a 1D chain). If we need to connect all the corresponding boundary qubits of the two parts, the overall success probability is exponentially small.

To overcome this problem, we introduce a method which enables efficient connection by attaching a long leg (a 1D cluster chain) to each boundary qubit of the 2D lattice. The protocol is divided into the following steps: First, we try to build a "+" shape cluster state by probabilistically connecting two cluster chains each of length $2n_l + 1$ (the value of n_l is specified below). This can be done through the probabilistic ZZ gate together with a simple Hadamard gate H and an X measurement, as shown in Fig. 2A and explained in its caption. With on average $1/p$ repetitions, we get a "+" shape state with the length of each of the four legs given by n_l. We use the "+" shape state as the basic building blocks of large scale 2D cluster states. In the "+" shape state, we have attached four long legs to the center qubit. The leg qubits serve as ancilla to generate near-deterministic connection from the probabilistic ZZ gates. The critical idea here is that if we want to connect two center qubits, we always start the connection along the end qubits of one of
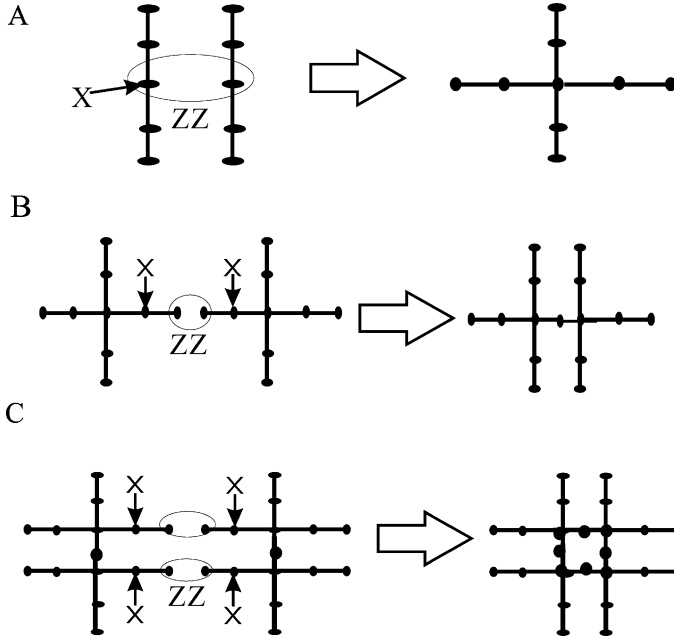
FIG. 11. Illustration of the steps for construction of the two-dimensional square lattice cluster states from a set of cluster chains. (A) Construction of the basic "+" shape states from cluster chains by applying a ZZ gate to connect the two middle qubits, and a X measurement on one middle qubit to remove it. (B) and (C): Construction of the square lattice cluster state from the "+" shape states through probabilistic ZZ gates along the legs and X measurements to remove the remaining redundant qubits. See Duan and Raussendorf (2005) for a similar construction with the controlled phase flip gates.

the legs (see illustration in Fig. 11). If such an attempt fails, we can delete two end qubits and try the connection again along the same legs. If the leg is sufficiently long, we can almost certainly succeed before we reach (destroy) the center qubits. When we succeed, and if there are still redundant leg qubits between the two center ones, we can delete the intermediate leg qubits by performing simple single-bit X measurements on all of them (see Figs. 11 and 10C for the third property of the cluster state). With such a procedure, we can continuously connect the center qubits and form any complex lattice geometry (see the illustration for construction of the square lattice state in Figs. 11B and C). What is important here is that after each time of connection of the center qubits, in the formed new shape, we still have the same length of ancillary legs on all the boundary qubits, which enables the succeeding near-deterministic connection of these new shapes.

Now we investigate for the 2D case how the computational overhead scales with the size of the cluster state. If the ancillary legs have length n_l, for each

connection of two center qubits, we can try at most $n_l/2$ times of the probabilistic ZZ gates, and the overall success probability is given by $p_c = 1 - (1 - p)^{n_l/2}$. If we want to build a square lattice cluster state of N qubits, we need about $2N$ times of connections of the center qubits (there are about $2N$ edges in an N-vertex square lattice). The probability for all these connections to be successful is given by p_c^{2N}. We require this overall success probability is sufficiently large with $p_c^{2N} \geqslant 1 - \epsilon$, where ϵ is a small number characterizing the overall failure probability. From that requirement, we find $n_l \simeq (2/p) \ln(2N/\epsilon)$. To construct a square lattice cluster state of N qubits, we need to consume N "+" shape states, and each of the latter requires on average $2/p$ cluster chains with a length of $2n_l + 1$ qubits. So we need in total $2N/p$ $(2n_l + 1)$-bit cluster chains, which can be prepared in parallel with $(2N/p)M(2n_l + 1)$ ZZ attempts within a time period $T(2n_l + 1)$ [see Eqs. (1) and (2) for expressions of the $M(n)$ and $T(n)$]. This gives the resources for preparation of all the basic building blocks (the chains). Then we need to connect these blocks to form the square lattice. We assume that the connection of all the building blocks are done in parallel. The whole connection takes on average $2N/p$ CPF attempts, and consumes a time at most $t_a/p \ln(2N/\epsilon)$. Summarizing these results, the temporal and the operational resources for preparation of an N-bit square lattice cluster state are approximately given by

$$T(N) \simeq t_a(1/p)^{\log_2(4/p-3)} + \frac{t_a}{p} \ln(2N/\epsilon)$$

$$+ \frac{t_a}{p} \log_2\left(\frac{4}{p}\left[\ln(2N/\epsilon) - 1\right]\right), \tag{22}$$

$$M(N) \simeq (2/p)^{2+\log_2(4/p-3)} N\left[\ln(2N/\epsilon) - 1\right] + 2N/p. \tag{23}$$

In the 2D case, the temporal and the operational overhead still have very efficient scaling with the qubit number N, logarithmically for $T(N)$ and $N \ln(N)$ for $M(N)$. Their scalings with $1/p$ are almost the same as in the 1D case except for an additional factor of $1/p^2$ for $M(N)$. Through some straightforward variations of the above method, it is also possible to efficiently prepare any complicated graph state using probabilistic ZZ gates. This shows that in principle we do not need to impose any threshold on the success probability of the ZZ gates for construction of efficient quantum computation. Although the probabilistic gate that we mentioned in the previous section succeeds only with a small probability in practice, it still provides a way to scalable quantum computation.

4.4. Experiments towards Probabilistic Ion Gates

4.4.1. *Ion–Photon Entanglement*

While matter–light entanglement has been implicit in many experimental systems over the past few decades (Haroche et al., 2002; Kuhn and Rempe, 2002;

McKeever et al., 2003; Freedman and Clauser, 1972; Aspect et al., 1982; Eichmann et al., 1993; DeVoe and Brewer, 1996; Kuzmich et al., 2000, 2003; Julsgaard et al., 2001; Van der Wal et al., 2003; Blinov et al., 2004; Moehring et al., 2004; Matsukevich and Kuzmich, 2004; Chou et al., 2005; Volz et al., 2006), atom–light entanglement is particularly clean in the ion trap system, where both atomic and photonic qubits are under great control. Early experiments involved the entanglement between the polarization of the photon with the hyperfine ground state of a trapped ion (Blinov et al., 2004; Moehring et al., 2004). Polarization qubits are more sensitive to decoherence from birefringence, and typically are useful only along certain directions of atomic emission. We therefore concentrate on the use of photonic frequency qubits, where the central frequency of the photon is entangled with the internal qubits state, as described above.

In a recent experiment, indirect evidence of the entanglement between an atomic qubit and a photon frequency qubit was demonstrated in the ^{111}Cd$^+$ system (Madsen et al., 2006). A diagram of the relevant energy levels and a description of the experiment are given in Fig. 12. First, the ion is optically pumped to $|0, 0\rangle \equiv |\uparrow\rangle$, and a microwave pulse prepares the ion in the state $(|\downarrow\rangle + |\uparrow\rangle)/\sqrt{2}$ [Fig. 12(a)]. Next, a single π-polarized ultrafast laser pulse coherently drives the superposition to the clock states in the $^2P_{3/2}$ manifold with near unit probability. The coherence in this excitation scheme is demonstrated using a microwave Ramsey experiment. In the absence of ultrafast laser pulses, the Ramsey contrast is essentially perfect. Following the application of the ultrafast laser pulse the atom is driven to the excited state. The excited atom then spontaneously decays, and without precise measurement of the photon polarization, frequency, and emission time, the coherence is lost, as seen in Fig. 12(e). The uncontrolled measurement of the photon results in tracing over the photon portion of the density matrix and the resulting loss in contrast is consistent with prior ion–photon entanglement.

To show that the excitation pulse is indeed coherently driving the superposition to the excited state, the Ramsey coherence is recovered by driving the ion back down to the ground state before spontaneous emission occurs [Fig. 12(c)]. With a pair of picosecond laser pulses incident on the ion between the microwave pulses, the contrast reappears with a phase shift proportional to the time Δt spent in the excited state and the hyperfine frequency difference between the ground and excited state levels: $\Delta t(\nu_0 - \nu_1) = (680 \text{ ps})(13.9 \text{ GHz}) = 18.9\pi$ [Fig. 12(e)]. The observed contrast is only 40% of the contrast without ultrafast laser pulses due to limited laser power in the second pulse and spontaneous decay ($\sim$23%) during the delay time between the ultrafast pulses.

4.4.2. Two Photon Interference

As mentioned previously, once two atoms are entangled with their respective photons, the next step for remote atom entanglement is the interference of the photon
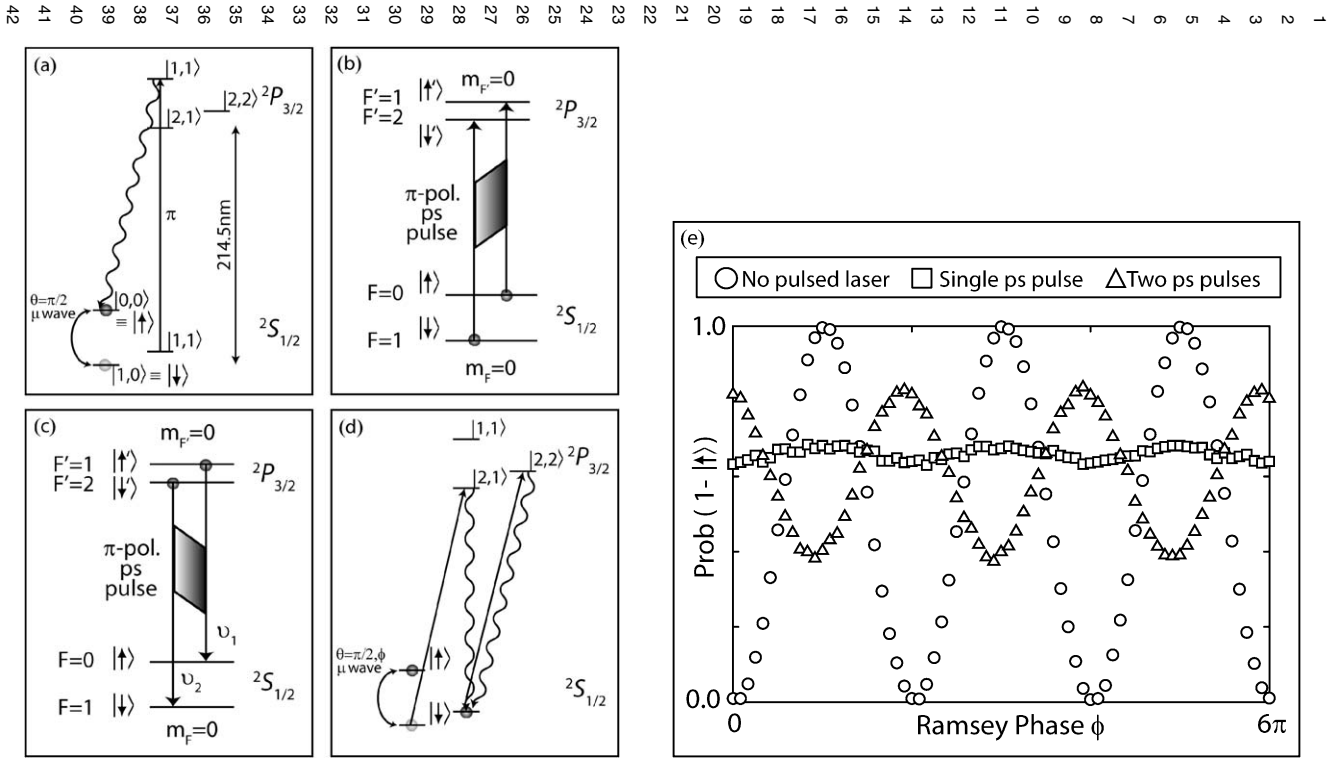
FIG. 12. Experimental procedure for atom–photon entanglement with photon frequency qubits (Madsen et al., 2006). (a) The ion is initialized in the state $(|\downarrow\rangle + |\uparrow\rangle)/\sqrt{2}$ via optical pumping to the $|0, 0\rangle$ state and a microwave $\pi/2$ pulse. (b) The superposition of atomic qubit states is coherently driven to the $^{2}P_{3/2}$ excited state via a resonantly tuned π-polarized ultrafast laser pulse. (c) A second pulse drives the qubit back to the ground state a short time later. (d) A second $\pi/2$ microwave pulse with variable phase completes the Ramsey experiment and the atomic state is measured using a resonance fluorescence technique. (e) Results from the microwave Ramsey experiment. Circles show the near perfect Ramsey fringes for the case with no ultrafast laser pulse. With a single ultrafast laser pulse, the coherence is lost due to the spontaneous emission of a photon that is not measured in a controlled, precisely timed fashion (squares). The average population in the bright state is above 0.5 due to the fluorescence branching ratios [Fig. 16(inset)]. Upon application of a second ultrafast laser pulse, the coherence in the ion is maintained by driving the qubit states back down to the ground states (triangles).
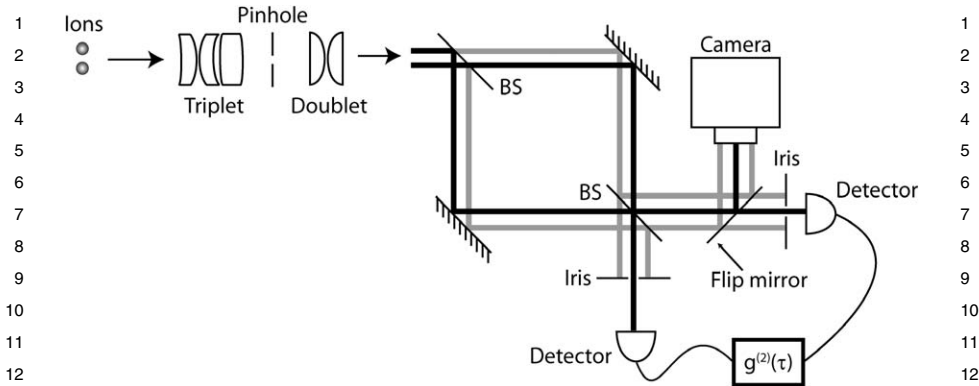
FIG. 13. Detection system for the two-photon interference experiment. The light from the two ions is separated on a beam splitter (*BS*) and mode-matched on the second *BS*. The photons are detected on single photon sensitive photomultiplier tubes (PMTs). A camera is used for coarse alignment, and the non-overlapping photon modes are blocked by irises.

modes from each atom on a beam splitter. Progress toward this end has been recently demonstrated (Beugnon et al., 2006; Maunz et al., 2006). In the cadmium ion system, two ions are placed in a trap and a beam-splitter setup is used to interfere the emitted photons (Fig. 13). In this setup, light scattered by the two ions is collected using an $f/2.1$ objective lens with a working distance of 13 mm. A pinhole is placed at the intermediate image for suppression of background photons and the intermediate image is re-imaged by a doublet lens. The image is then broken up into two paths by a beam splitter, and the transmitted and reflected beam pairs are directed to a second beam splitter where the light from each ion is superimposed. Irises are used to block the unwanted beams and the overlapping beams are directed to photomultiplier tubes (PMTs) with a time resolution of about 1 ns (Moehring et al., 2006). The equal path lengths of the transmitted and reflected beams ensure that the photons emitted by two ions are mode-matched in size and divergence. Coarse alignment is performed by imaging the light after the second beam splitter on a single photon sensitive camera, where the overall magnification of the imaging system is about 1000 and the diffraction-limited image of the two ions are separated by 2 mm, each with a spot size of 0.5 mm.

To demonstrate two photon interference, first the photon statistics of a single ion excited by a σ^+-polarized cw laser is investigated (dashed line in Fig. 14). In this case, the $g^{(2)}$ autocorrelation function shows the expected damped Rabi oscillations (Diedrich and Walther, 1987; Itano et al., 1988) between the $^2S_{1/2}|1, 1\rangle$ and $^2P_{3/2}|2, 2\rangle$ levels. It is unlikely that two photons are emitted from one ion in close proximity since after emission of a single photon, the ion is assured to be in the ground state. The maximum observed antibunching for the single ion
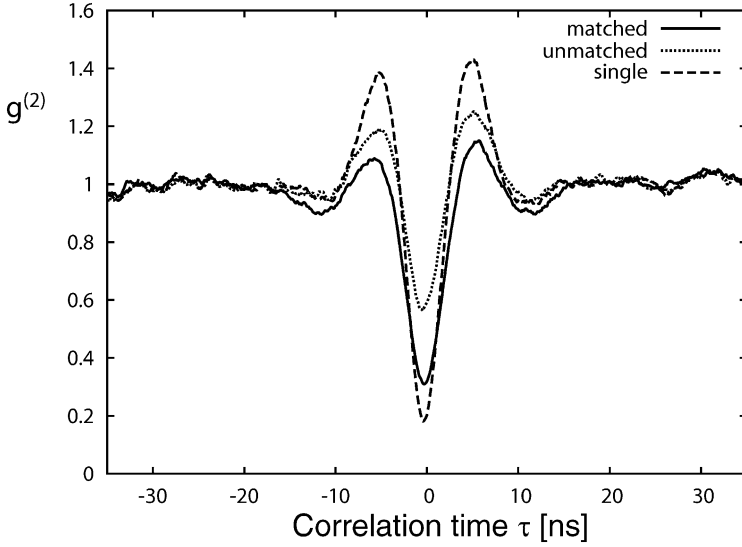
FIG. 14. Intensity autocorrelation for cw-excitation. The dashed line shows strong antibunching for a single ion with $g_1^{(2)}(0) = 0.18$, limited by the resolution of the detection system. With this value, the expected antibunching of light from two non-overlapping ions is expected to be $g_{2,um}^{(2)}(0) = 0.59$ in good agreement with the experimental value (dotted line). If the two photon modes are matched, the interference leads to a significant reduction of coincidence detections (solid line). The measured antibunching was $g_{2,m}^{(2)}(0) = 0.31$, corresponding to a mode overlap of about 57%.

is $g_1^{(2)}(0) = 0.18$ as expected for the time resolution of the PMTs (Maunz et al., 2006).

Next, two ions are illuminated equally and purposefully not mode-matched on the beam splitter. In this case, half of the signal results from two photons from the same ion, and the other half result from one photon from each ion. Since these photon modes are not matched on the beam splitter, the detected photons are uncorrelated. We therefore expect a reduced antibunching,

$$g_{2,um}^{(2)}(0) = \frac{1}{2}\big(1 + g_1^{(2)}(0)\big) \approx 0.59,$$

in agreement with the measurement (dotted line in Fig. 14).

If the photon modes from each ion are matched on the beam splitter, then the photons always leave on the same output port, and thus no coincident detections are observed (Mandel, 1999). The suppression of coincidence events is clearly visible in the autocorrelation signal of the mode-matched ions (solid line in Fig. 14) and has a measured $g_{2,m}^{(2)}(0)$ of 0.31. This corresponds to an interference signal of about 57% (amplitude matching of 75%), and compares well to the results observed in reference (Beugnon et al., 2006). This mode overlap is not

ideal and is likely due to phase front distortions from the two atomic sources as they sample different parts of many optical surfaces before finally interfering on the beam splitter.

In order to entangle two remotely located atoms, it is likely necessary to use single mode optical fibers. This is because interfering the two photon modes requires very high stability of the atom and collection optics with respect to the beam splitter, as well as good spatial mode matching from the two imaging systems. With free-space mode-matching, any relative motion of the trapped atoms and the imaging optics can ruin the entanglement fidelity by producing false positive detection events, while in the fiber coupled case, effects such as mechanical vibrations and thermal drifts simply lower the rate of coincidence counts (ignoring dark counts). In the cadmium system, however, the spontaneously emitted photons are deep in the ultraviolet at 214.5 nm where it is very difficult to use optical fibers. Very recently, single photons emitted from two remotely-located Yb^+ ions have been interfered using optical fiber, resulting in better than 80% contrast in the two-photon coincidence rate.

4.4.3. Single Photon Sources

It is important for the atoms to emit only a single photon during an entanglement trial, especially with remote-atom entanglement. Such a single photon source was demonstrated recently using optical excitation of a single cadmium ion with a picosecond mode-locked Ti:sapphire laser (Maunz et al., 2006). This laser is tuned to 858 nm and is sent through a pulse picker to reduce the repetition rate from 81 MHz to 27 MHz with an extinction ratio of better than 100:1 in the infrared. The pulses are frequency quadrupled through single pass nonlinear crystals and the resulting 214.5 nm laser pulses have a pulse extinction ratio near 10^{-8} and a transform-limited pulse width of about 1 ps. This allows excitation of the ion on a timescale much faster than the 2.65 ns excited state lifetime.

The single ion is repeatedly excited with the pulsed laser resulting in a periodic emission of photons at the laser pulse separation time of 37.5 ns, and the intensity autocorrelation function of the photons is recorded using a multi-channel scaler (Fig. 15). The half width of each peak is given by the excited state lifetime and the peak at zero time delay corresponding to coincidentally detected photons is almost entirely suppressed. This near-perfect antibunching is highly non-classical and demonstrates that at most one photon is emitted from the ion following an excitation pulse (limited by the possibility of emitting and detecting a photon *during* the excitation pulse $\approx 10^{-6}$). The residual peak at zero time delay has a height of about 2% of the other peaks, originating from diffuse scattered light from the pulsed laser. With fast electronics, this residual peak could be identically zero by vetoing photons emitted during the picosecond laser pulse.

The use of ultrafast lasers also allows unit-probability excitation ($p_e \sim 1$) while maintaining a single photon source. This corresponds to performing a Rabi π
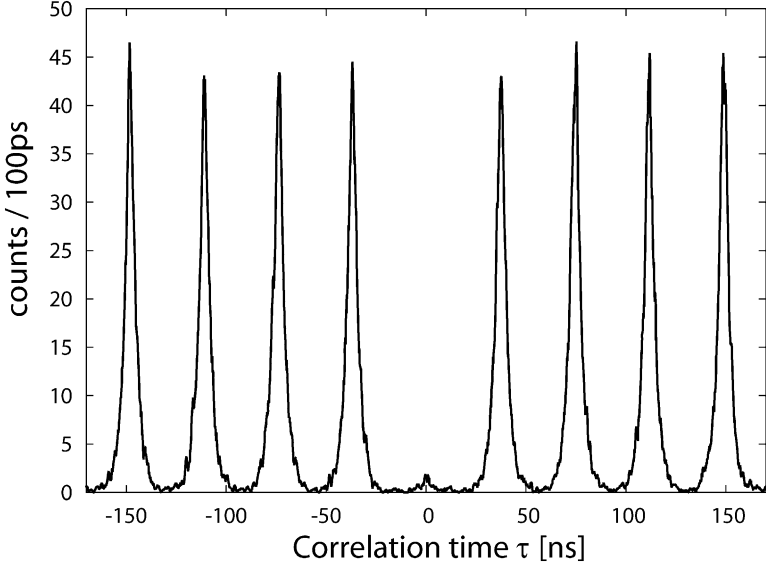
FIG. 15. Intensity autocorrelation of the light emitted by a single ion excited by an ultrafast laser. The near perfect antibunching at $t = 0$ shows that at most one photon is emitted from an excitation pulse.

pulse on the optical S–P transition. In a recent experiment, the Rabi angle was measured by preparing the ion in a known initial ground state and applying a single excitation pulse of known polarization (Madsen et al., 2006). With knowledge of the fluorescence branching ratios and the ability to perform efficient state detection, Rabi flopping with the pulsed laser can be detected using every laser pulse with a high signal to noise ratio (Fig. 16). An alternative method would be to detect the photon scattering rate from an ion as a function of the pulse energy where Rabi angles with an odd (even) multiple of π would have a maximum (minimum) of scattered photons as the ion would be left in the excited (ground) state at the end of each pulse (Darquie et al., 2005).

In the experiment, the ion is prepared in the $|0, 0\rangle$ ground state through optical pumping (Lee et al., 2003). A single linearly polarized ps laser pulse excites the ion to the $P_{3/2}|1, 0\rangle$ state. After a time (10 μs) much longer than the excited state lifetime, the ion has decayed back to the $S_{1/2}$ ground state levels via spontaneous emission following the fluorescence branching ratios. The atomic ground states are then measured using resonance fluorescence detection where all three $F = 1$ states are equally bright, while the $F = 0$ state is dark (Blatt and Zoller, 1988; Lee et al., 2005; Acton et al., 2006), with the results shown in Fig. 16. The available power from the pulsed laser limits the Rabi rotation angle to roughly π, and the
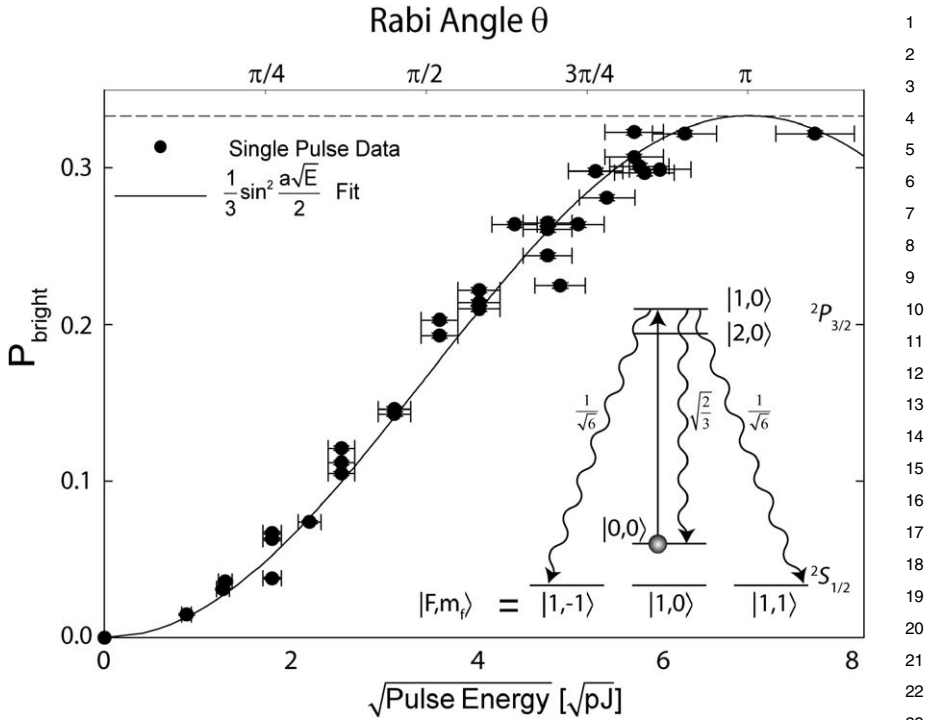
FIG. 16. The ion bright state population as a function of pulse energy. Each point represents a collection of 60,000 runs. As the population in the excited P state is driven to unity, the bright state population approaches 1/3 (horizontal dashed line), determined by the spontaneous emission branching ratio. The data are fit to a single parameter giving a value $a = 0.42$ pJ$^{-1/2}$. Inset: Relevant energy levels for the $S-P$ Rabi oscillation experiment. A π-polarized ultrafast laser pulse excited the ion from the ground state to the excited state with variable energy. The three possible decay channels are shown with their respective fluorescence branching ratios. After a time (10 μs) following the excitation pulse, the bright state population of the ion was measured using resonance fluorescence detection.

data agree well with the estimates based on the beam waist, pulse length and pulse shape (Madsen et al., 2006). The probability of measuring the bright state is equal to 1/3 the probability of excitation to the excited state, as follows from the Clebsch–Gordan coefficients [Fig. 16(inset)]. Hence, we have shown that unit excitation and single photon emission can be achieved with ultrafast laser pulses.

5. Summary

In this article, we have reviewed several schemes towards the goal to realize scalable quantum communication, state engineering, and quantum computation with

different physical systems, including atomic ensembles, photons under linear optical devices, and trapped atoms or ions. For all of these schemes, we can reduce the dominant experimental noise to particular types of errors, and then correct such errors at a arbitrarily high level. As a result, these schemes are inherently immune to these special sources of error. This inherent insensitivity to noise opens up a practical route for realization of scalable quantum information with realistic physical devices. Examples of experimental progress along these lines have been described.

6. Acknowledgements

Uncited references

(Bose et al., 1999) (Cabrillo et al., 1999) (Cirac et al., 1997) (Collins et al., 2006) (Duan and Kimble, 2004) (Zukowski et al., 1993)

7. References

Acton, M., Brickman, K.-A., Haljan, P., Lee, P.J., Deslauriers, L., Monroe, C. (2006). Near-perfect simultaneous measurement of a qubit register. *Quant. Inf. Comp.* **6**, 465–482.

Aspect, A., Grangier, P., Roger, G. (1982). Experimental realization of Einstein–Podolsky–Rosen– Bohm *Gedankenexperiment*: A new violation of Bell's inequalities. *Phys. Rev. Lett.* **49**, 91–94.

Balic, V., Braje, D.A., Kolchin, P., Yin, G.Y., Harris, S.E. (2005). Generation of paired photons with controllable waveforms. *Phys. Rev. Lett.* **94**, 183601–183604.

Barrett, S.D., Kok, P. (2005). Efficient high-fidelity quantum computation using matter qubits and linear optics. *Phys. Rev. A* **71R**. 060310.

Bennett, C.H., et al. (1993). Teleporting an unknown quantum state via dual classical and Einstein–Podolsky–Rosen channels. *Phys. Rev. Lett.* **73**, 3081–3084.

Bennett, C.H., et al. (1997). Purification of noisy entanglement and faithful teleportation via noisy channels. *Phys. Rev. Lett.* **76**, 722–725.

Beugnon, J., Jones, M.P.A., Dingjan, J., Darquie, B., Messin, G., Browaeys, A., Grangier, P. (2006). Quantum interference between two single photons emitted by independently trapped atoms. *Nature* **440**, 779–782.

Black, A.T., Thompson, J.K., Vuletic, V. (2005). On-demand superradiant conversion of atomic spin gratings into single photons with high efficiency. *Phys. Rev. Lett.* **95**. 133601.

Blatt, R., Zoller, P. (1988). Quantum jumps in atomic systems. *Eur. J. Phys.* **9**, 250–256.

Blinov, B.B., Moehring, D.L., Duan, L.-M., Monroe, C. (2004). Observation of entanglement between a single trapped atom and a single photon. *Nature* **428**, 153–157.

Boschi, D., Branca1, S., De Martini, F., Hardy, L., Popescu, S. (1998). Experimental realization of teleporting an unknown pure quantum state via dual classical and Einstein–Podolsky–Rosen channels. *Phys. Rev. Lett.* **80**, 1121–1124.

Bose, S., Knight, P.L., Plenio, M.B., Vedral, V. (1999). Proposal for teleportation of an atomic state via cavity decay. *Phys. Rev. Lett.* **83**, 5158–5161.

Bouwmeester, D., et al. (1997). Experimental quantum teleportation. *Nature* **390**, 575–579.

Briegel, H.-J., Duer, W., Cirac, J.I., Zoller, P. (1998). Quantum repeaters: The role of imperfect local operations in quantum communication. *Phys. Rev. Lett.* **81**, 5932–5935.

Browne, D.E., Rudolph, T. (2005). Resource-efficient linear optical quantum computation. *Phys. Rev. Lett.* **95**, 010501–010504.

Cabrillo, C., Cirac, J.I., G-Fernandez, P., Zoller, P. (1999). Creation of entangled states of distant atoms by interference. *Phys. Rev. A* **59**, 1025–1033.

Chaneliere, T., Matsukevich, D.N., Jenkins, S.D., Lan, S.-Y., Kennedy, T.A.B., Kuzmich, A. (2005). Storage and retrieval of single photons transmitted between remote quantum memories. *Nature* **438**, 833–836.

Childress, L., Taylor, J.M., Sorensen, A.S., Lukin, M.D. (2006). Fault-tolerant quantum communication based on solid-state photon emitters. *Phys. Rev. Lett.* **96**. 070504.

Chou, C.W., Polyakov, S.V., Kuzmich, A., Kimble, H.J. (2004). Single-photon generation from stored excitation in an atomic ensemble. *Phys. Rev. Lett.* **92**, 213601–213604.

Chou, C.W., de Riedmatten, H., Felinto, D., Polyakov, S.V., van Enk, S.J., Kimble, H.J. (2005). Measurement-induced entanglement for excitation stored in remote atomic ensembles. *Nature* **438**, 828–832.

Cirac, J.I., Zoller, P., Kimble, H.J., Mabuchi, H. (1997). Quantum state transfer and entanglement distribution among distant nodes in a quantum network. *Phys. Rev. Lett.* **78**, 3221–3224.

Cirac, J.I., Duan, L.-M., Zoller, P. (2001). Quantum optical implementation of quantum information processing. In: *Proceedings of International School of Physics "Enrico Fermi" Courses*. See also quant-ph/0405030.

Collins, O.A., Jenkins, S.D., Kuzmich, A., Kennedy, T.A.B. (2006). Multiplexed memory-insensitive quantum repeaters. quant-ph/0610036.

Darquie, B., Jones, M.P.A., Dingjan, J., Beugnon, J., Bergamini, S., Sortais, Y., Messin, G., Browaeys, A., Grangier, P. (2005). Controlled single-photon emission from a single trapped two-level atom. *Science* **309**, 454–456.

Dawson, C.M., Haselgrove, H.L., Nielsen, M.A. (2006). Noise thresholds for optical quantum computers. *Phys. Rev. Lett.* **96**, 020501–020504.

DeVoe, R.G., Brewer, R.G. (1996). Observation of superradiant and subradiant spontaneous emission of two trapped ions. *Phys. Rev. Lett.* **76**, 2049–2052.

Diedrich, F., Walther, H. (1987). Nonclassical radiation of a single stored ion. *Phys. Rev. Lett.* **58**, 203–206.

Duan, L.-M. (2002). Entangling many atomic ensembles through laser manipulation. *Phys. Rev. Lett.* **88**, 170402–170405.

Duan, L.-M., Kimble, J. (2004). Scalable photonic quantum computation through cavity assisted interaction. *Phys. Rev. Lett.* **92**, 127902–127905.

Duan, L.-M., Raussendorf, R. (2005). Efficient quantum computation with probabilistic quantum gates. *Phys. Rev. Lett.* **95**, 080503–080506.

Duan, L.-M., Cirac, J.I., Zoller, P., Polzik, E.S. (2000). Quantum communication between atomic ensembles using coherent light. *Phys. Rev. Lett.* **85**, 5643–5646.

Duan, L.-M., Lukin, M.D., Cirac, J.I., Zoller, P. (2001). Long distance quantum communication with atomic ensembles and linear optics. *Nature* **414**, 413–418.

Duan, L.-M., Cirac, J.I., Zoller, P. (2002). Three-dimensional theory for interaction between atomic ensembles and free-space light. *Phys. Rev. A* **66**. 023818. 13 pp.

Duan, L.-M., Blinov, B.B., Moehring, D.L., Monroe, C. (2004). Scalable trapped ion quantum computation with a probabilistic ion–photon mapping. *Quant. Inf. Comp.* **4**, 165–173.

Duan, L.-M., Wang, B., Kimble, J. (2005). Robust quantum gates on neutral atoms with cavity-assisted photon-scattering. *Phys. Rev. A* **72**. 032333.

Duan, L.-M., Madsen, M.J., Moehring, D.L., Maunz, P., Kohn, R.N., Monroe, C. (2006). Probabilistic quantum gates between remote atoms through interference of optical frequency qubits. *Phys. Rev. A* **73**. 062324.

Eichmann, U., Bergquist, J.C., Bollinger, J.J., Gilligan, J.M., Itano, W.M., Wineland, D.J., Raizen, M.G. (1993). Young's interference experiment with light scattered from two atoms. *Phys. Rev. Lett.* **70**, 2359–2362.

Eisaman, M.D., Andre, A., Massou, F., Fleischhauer, M., Zibrov, A.S., Lukin, M.D. (2005). Electromagnetically induced transparency with tunable single-photon pulses. *Nature* **438**, 837–841.

Ekert, A. (1991). Quantum cryptography based on Bell's theorem. *Phys. Rev. Lett.* **67**, 661–663.

Fleischhauer, M., Lukin, M.D. (2000). Dark-state polaritons in electromagnetically induced transparency. *Phys. Rev. Lett.* **84**, 5094–5097.

Freedman, S.J., Clauser, J.F. (1972). Experimental test of local hidden-variable theories. *Phys. Rev. Lett.* **28**, 938–941.

Hein, M., Dür, W., Eisert, J., Raussendorf, R., Van den Nest, M., Briegel, H.-J. (2006). Entanglement in graph states and its applications. quant-ph/0602096.

Haroche, S., Raimond, J.M., Brune, M. (2002). In: *Experimental Quantum Computation and Information*. IOS Press, Amsterdam, pp. 3–36.

Itano, W.M., Bergquist, J.C., Wineland, D.J. (1988). Photon antibunching and sub-Poissonian statistics from quantum jumps in one and two atoms. *Phys. Rev. A* **38**, 559–562.

Julsgaard, B., Kozhekin, A., Polzik, E.S. (2001). Experimental long-lived entanglement of two macroscopic objects. *Nature* **413**, 400–403.

Knill, E., Laflamme, R., Milburn, G.J. (2001). A scheme for efficient quantum computation with linear optics. *Nature* **409**, 46–52.

Kuhn, A., Rempe, G. (2002). In: *Experimental Quantum Computation and Information*. IOS Press, Amsterdam, pp. 37–66.

Kuzmich, A., Mandel, L., Bigelow, N.P. (2000). Generation of spin squeezing via continuous quantum nondemolition measurement. *Phys. Rev. Lett.* **85**, 1594–1597.

Kuzmich, A., Bowen, W.P., Boozer, A.D., Boca, A., Chou, C.W., Duan, L.-M., Kimble, H.J. (2003). Generation of nonclassical photon pairs for scalable quantum communication with atomic ensembles. *Nature* **423**, 731–734.

Kwiat, P.G., Mattle, K., Weinfurter, H., Zeilinger, A., Sergienko, A.V., Shih, Y.H. (1995). New high-intensity source of polarization-entangled photon pairs. *Phys. Rev. Lett.* **75**, 4337.

Lee, P.J., Blinov, B.B., Brickman, K.-A., Deslauriers, L., Madsen, M.J., Miller, R., Moehring, D.L., Stick, D., Monroe, C. (2003). Atomic qubit manipulations with an electro–optic modulator. *Optics Letters* **28**, 1582–1584.

Lee, P.J., Brickman, K.-A., Deslauriers, L., Haljan, P.C., Duan, L.-M., Monroe, C. (2005). Phase control of trapped ion quantum gates. *Journal of Optics B* **7**, S371–S383.

Lim, Y.L., Barrett, S.D., Beige, A., Kok, P., Kwek, L.C. (2006). Repeat-until-success quantum computing using stationary and flying qubits. *Phys. Rev. A* **73**. 012304.

Liu, C., Dutton, Z., Behroozi, C.H., Hau, L.V. (2001). Observation of coherent optical information storage in an atomic medium using halted light pulses. *Nature* **409**, 490–493.

Lu, C.-Y., et al. (2006). Experimental entanglement of six photons in graph states. quant-ph/0609130.

Lukin, M.D. (2003). Colloquium: Trapping and manipulating photon states in atomic ensembles. *Rev. Mod. Phys.* **75**, 457–472.

McKeever, J., Buck, J.R., Boozer, A.D., Kuzmich, A., Nagerl, H.-C., Stamper-Kurn, D.M., Kimble, H.J. (2003). State-insensitive cooling and trapping of single atoms in an optical cavity. *Phys. Rev. Lett.* **90**, 133602–133605.

Madsen, M.J., Moehring, D.L., Maunz, P., Kohn Jr., R.N., Duan, L.-M., Monroe, C. (2006). Ultrafast coherent coupling of atomic hyperfine and photon frequency qubits. *Phys. Rev. Lett.* **97**, 040505–040508.

Mandel, L. (1999). Quantum effects in one-photon and two-photon interference. *Rev. Mod. Phys.* **71**, S274–S282.

Manz, S., Fernholz, T., Schmiedmayer, J., Pan, J.-W. (2006). Collisional decoherence during writing and reading quantum states. quant-ph/0608159.

Matsukevich, D.N., Kuzmich, A. (2004). Quantum state transfer between matter and light. *Science* **306**, 663.

Matsukevich, D.N., Chaneliere, T., Jenkins, S.D., Lan, S.-Y., Kennedy, T.A.B., Kuzmich, A. (2006). Entanglement of remote atomic qubits. *Phys. Rev. Lett.* **96**, 030405–030408.

Maunz, P., Moehring, D.L., Madsen, M.J., Kohn Jr., R.N., Younge, K.C., Monroe, C. (2006). Quantum interference of photon pairs from two trapped atomic ions. quant-ph/0608047.

Moehring, D.L., Madsen, M.J., Blinov, B.B., Monroe, C. (2004). Experimental Bell inequality violation with an atom and a photon. *Phys. Rev. Lett.* **93**, 090410–090413.

Moehring, D.L., Blinov, B.B., Gidley, D.W., Kohn Jr., R.N., Madsen, M.J., Sanderson, T.B., Vallery, R.S., Monroe, C. (2006). Precision lifetime measurement of a single trapped ion with ultrafast laser pulses. *Phys. Rev. A* **73**. 023413.

Monroe, C. (2002). Quantum information processing with atoms and photons. *Nature* **416**, 238–246.

Nielsen, M.A. (2004). Optical quantum computation using cluster states. *Phys. Rev. Lett.* **93**, 040503–040506.

Nielsen, M.A., Chuang, I.L. (2000). "Quantum Computation and Quantum Information". Cambridge University Press.

Pan, J.-W., Daniell, M., Gasparoni, S., Weihs, G., Zeilinger, A. (2001). Experimental demonstration of four-photon entanglement and high-fidelity teleportation. *Phys. Rev. Lett.* **86**, 4435–4438.

Phillips, D.F., et al. (2001). Storage of light in atomic vapor. *Phys. Rev. Lett.* **86**, 783–786.

Preskill, J. (1998). Reliable quantum computers. *Proc. R. Soc. Lond. A* **454**, 385–410.

Raussendorf, R., Briegel, H.J. (2001). A one-way quantum computer. *Phys. Rev. Lett.* **86**, 5188–5191.

Riedmatten, H., Laurat, J., Chou, C.W., Schomburg, E.W., Felinto, D., Kimble, H.J. (2006). Direct measurement of decoherence for entanglement between a photon and stored atomic excitation. *Phys. Rev. Lett.* **97**, 113603–113606.

Shi, Y.-Y., Duan, L.-M., Vidal, G. (2006). Classical simulation of quantum many-body systems with a tree tensor network. *Phys. Rev. A* **74**. 022320.

Shor, P.W. (1995). Scheme for reducing decoherence in quantum computer memory. *Phys. Rev. A* **52**. R2493.

Steane, A.M. (1997). Error correcting codes in quantum theory. *Phys. Rev. Lett.* **77**, 793.

Van der Wal, C.H., Eisaman, M.D., Andr, A., Walsworth, R.L., Phillips, D.F., Zibrov, A.S., Lukin, M.D. (2003). Atomic memory for correlated photon states. *Science* **301**, 196.

Volz, J., Weber, M., Schlenk, D., Rosenfeld, W., Vrana, J., Saucke, K., Kurtsiefer, C., Weinfurter, H. (2006). Observation of entanglement of a single photon with a trapped atom. *Phys. Rev. Lett.* **96**, 030404–030407.

Walther, P., et al. (2005). Experimental one-way quantum computing. *Nature* **434**, 169–176.

Yoran, N., Reznik, B. (2003). Deterministic linear optics quantum computation with single photon qubits. *Phys. Rev. Lett.* **91**, 037903–037906.

Zukowski, M., Zeilinger, A., Horne, M.A., Ekert, A. (1993). "Event-ready-detectors" Bell experiment via entanglement swapping. *Phys. Rev. Lett.* **71**, 4287–4290.